Geochemistry, Geophysics, Geosystems®

AGU ADVANCING EARTH AND SPACE SCIENCE

RESEARCH ARTICLE
10.1029/2021GC010230

Intrusive Magmatism Strongly Contributed to the Volatile Release Into the Atmosphere of Early Earth

Sara Vulpius[1] **and Lena Noack**[1]

[1]Department of Earth Sciences, Freie Universität Berlin, Berlin, Germany

Key Points:

- In our model, we quantify the release of H_2O and CO_2 from a magma body and its significance for early Earth
- We examine the effect of fractional crystallization on the solubility and release of volatiles
- We consider the buoyancy of the melt and the formation of hydrous minerals

Supporting Information:

Supporting Information may be found in the online version of this article.

Correspondence to:

S. Vulpius,
sara.vulpius@fu-berlin.de

Citation:

Vulpius, S., & Noack, L. (2022). Intrusive magmatism strongly contributed to the volatile release into the atmosphere of early Earth. *Geochemistry, Geophysics, Geosystems*, *23*, e2021GC010230. https://doi.org/10.1029/2021GC010230

Received 25 OCT 2021
Accepted 5 JUN 2022

Abstract Magmatic volatile release was crucial for the build-up and composition of the early atmosphere and thus for the origin and evolution of life. Even though the rate of intrusive to extrusive magma production on Earth is high, intrusive volatile release is commonly neglected in studies modeling the composition of the early atmosphere. This can mainly be attributed to the solubility of volatiles like H_2O and CO_2. The solubility is increasing with depth and thus is thought to prevent the release of these volatiles. However, due to the accumulation of H_2O and CO_2 within the melt during fractional crystallization, the solubility can be exceeded even at greater depths. In our study, we developed a novel numeric model to quantify the amount of H_2O and CO_2 that can be released from an intrusive system if we consider the process of fractional crystallization. Additionally, we take the possibility of melt ascent and the formation of hydrous minerals into account. According to our simulations, the release of H_2O and CO_2 from an intrusive magma body is possible within the whole lithosphere. However, the release strongly depends on the initial volatile budget, the formation of hydrous phases, the depth of the intrusion and the buoyancy of the melt. Considering all these factors, our study suggests that about 0%–85% H_2O and 100% CO_2 can be released from mafic intrusions. This renders the incorporation of the intrusive volatile release mandatory in order to determine the volatile fluxes and the composition of early Earth's atmosphere.

1. Introduction

The major source of Earth's atmosphere is the volatile release from the interior, at least since the late Hadean. Earlier stages of the atmosphere include the primordial atmosphere accreted from the solar nebular, and the primary atmosphere outgassed from the Hadean magma ocean (Ortenzi et al., 2020; Van Hoolst et al., 2019). Both were lost to space, at least to a large extent, by hydrodynamic escape and impact erosion (e.g., Gaillard & Scaillet, 2014; Lammer et al., 2008; Zahnle et al., 2010). The build-up, density and composition of the secondary atmosphere on early Earth was crucial for the emergence and evolution of life (e.g., Gargaud et al., 2013; Miller, 1953). Since these factors depend on the volatiles released from the interior, the amount and composition of the volatiles are essential and require detailed investigation.

It is assumed that today intrusive magma production rates are significantly higher compared to extrusive rates (Crisp, 1984; Shinohara, 2008) and were probably also considerably higher during the Archean (Jain et al., 2019; Lourenço et al., 2018, 2020; Rozel et al., 2017). Therefore, intrusive volatile release is a crucial process in the examination of Earth's atmosphere. While recent models have focused extensively on extrusive outgassing (e.g., Dorn et al., 2018; Grott et al., 2011; Kite et al., 2009; Noack et al., 2017; Ortenzi et al., 2020), intrusive volatile release is often neglected when estimating the outgassing fluxes of early atmospheres. However, there are some studies addressing the topic of intrusive volatile release (e.g., Degruyter et al., 2019; Edmonds et al., 2022; McKay et al., 2014; Nava et al., 2021; Parmigiani et al., 2017). McKay et al. (2014) and Nava et al. (2021) attempted to match proxies of climate changes coinciding with large igneous provinces (LIPs) by considering the impact of intrusive outgassing. To link these events, they applied different approaches. McKay et al. (2014) simulated the influence of the Columbia River Basalts accounting for intrusive ("cryptic") degassing by adding a factor of 2.0–6.4 to the extrusive outgassing of the sub-aerial basalts. Nava et al. (2021) measured the CO_2 content of melt inclusions, the bubbles trapped in these inclusions as well as the CO_2/Ba and CO_2/Nb ratios of the Deccan Traps. The measurements are used to reconstruct the initial CO_2 content of the melt. Both studies infer that extrusive outgassing alone is insufficient to cause the climate change following the LIP eruptions. However, if the intrusive release of volatiles is accounted for, LIPs could at least partially explain the climate change. These studies represent meaningful contributions to the significance of intrusive volatile release, although they lack a detailed investigation of the formation of the volatile phase itself, particularly at high pressures. Parmigiani

et al. (2017) and Degruyter et al. (2019) focused on modeling the possibility of gas bubble migration and channel formation, considering mainly the spatial and volumetric distribution between bubbles and crystals. Their results show that at least half of the initial H_2O is lost within a crystal fraction range of 0.4–0.7 at 0.2 GPa. This work provides important insights into the process of intrusive degassing. Although, it would be necessary to examine the entire crystallization process for a wider pressure range determining the total release of the volatiles from intrusions. Neither of the studies mentioned above consider the effect of fractional crystallization and volatile solubility on the volatile release which is necessary to quantify the contribution of intrusive volatile release to the total outgassing.

One reason why intrusive volatile release has often been neglected in previous models is the high solubility of the volatiles, such as H_2O and CO_2. At high pressure, they are completely dissolved in the melt and unable to be released (e.g., Gaillard & Scaillet, 2014; Iacono-Marziano et al., 2012; Parfitt & Wilson, 2008). However, one could postulate that this might be different when considering the effect of fractional crystallization. Due to cooling, nominally mafic minerals precipitate and deplete the residual melt in compatible elements. Instead, incompatible elements and molecules (including volatiles) cannot be incorporated into the crystal lattice of nominally mafic minerals due to their large ionic radius and/or charge. Thus, the volatiles accumulate within the melt. The progressive enrichment of the volatiles in the melt leads to oversaturation and to the exsolution of a volatile phase (e.g., Holloway & Blank, 1994; Parfitt & Wilson, 2008; Petrelli et al., 2018; Wallace et al., 1995; Zhang et al., 2007) even at high pressures. This exsolved volatile phase is buoyant and we assume that it ascends through already existing cracks and fissures or generates new cracks due to its own overpressure. This way, the released volatiles could reach the surface to contribute to the composition of the atmosphere.

The aim of this study is to quantify the effect of fractional crystallization during magma body crystallization on the volatile release. For this purpose, we developed a novel numerical model to simulate the release of H_2O and CO_2. In contrast to previous studies, we examine the formation of a volatile phase by considering (a) the effects of fractional crystallization in combination with the solubility of the volatiles, and (b) the concurrent formation of hydrous phases as well as the influence of the volatiles on the buoyancy of the melt. We compare the impact of these mechanisms on the volatile release and discuss the likelihood of a volatile phase reaching the surface. We present the resulting volatile release efficiencies depending on our model assumptions for the entire pressure range of the lithosphere (10^{-4} to 3 GPa) and the whole crystallization process from liquidus to solidus. Finally, we quantify the contribution of the intrusive volatile release to the total magmatic outgassing flux. This quantification is essential for further studies to improve the determination of the composition and development of the secondary atmosphere. Our model can be applied to any possible scenario related to intrusions, whether on a local scale, such as the formation of ore deposits or the impact of intrusive volatile release at a particular location, or on a global scale, such as the determination of volatile fluxes and cycles on the early Earth and today.

2. Methods

In this study, we quantify the amount of volatiles that can be released from an emplacement of a basaltic magma body within the lithosphere by applying our newly developed numerical model. It is thought that the Earth's uppermost mantle has had a similar oxidation state as today, at least since the early Archean (e.g., Canil, 1997; Delano, 2001; Li & Lee, 2004; Scaillet & Gaillard, 2011; Trail et al., 2011). For this reason, the release of hydrogen and carbon within the lithosphere can be constrained to the oxidizing species H_2O and CO_2. In our model, we exclusively consider basaltic melts. The effect of fractional crystallization on the distribution of the major components between the liquid an the solid is neglected for simplicity (except for H_2O and CO_2). However, the potential implications of using a more complex model that accounts for this process are discussed in Section 4.

First, we describe the implementation of fractional crystallization and release of volatiles upon exceeding solubility. We then describe different elements of increasing complexity within our model, including the determination of melt buoyancy as well as the formation of hydrous minerals. Our model is implemented in and evaluated with MATLAB, but any other programming language is equally suitable.

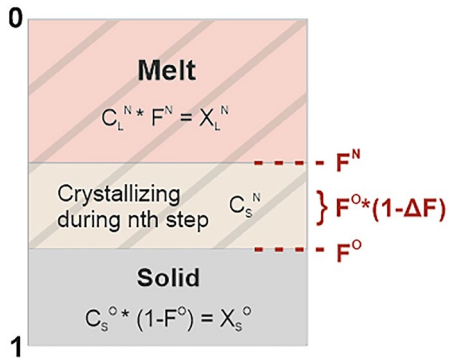

Figure 1. Sketch of the process of fractional crystallization including the main equations of this study. The numbers on the left indicate the melt fraction at the beginning ($F = 1$) and at the end ($F = 0$) of a complete crystallization process. F^N is the new melt fraction of each iteration step, while F^O is the old melt fraction from the previous step. ΔF is a pre-defined increment (e.g., 0.01) by which the melt fraction F^O is reduced in each iteration step. The yellowish area (in the middle) represents C_S^N, which is the concentration of H_2O or CO_2 in the solid that is just crystallizing during the current iteration step. The gray area (at the bottom) represents the added-up amount of H_2O or CO_2 in the solid from previous simulation steps $\left(C_S^O\right)$. C_S^O multiplied by $1 - F^O$ yields the volume-dependent total concentration of H_2O or CO_2 stored in the solid material expressed as a whole system from all previous iteration steps. The reddish area (at the top) represents the new concentration of H_2O or CO_2 in the liquid of the current iteration step $\left(C_L^N\right)$. Multiplying C_L^N with the new melt fraction F^N equals the volume-dependent total concentration of H_2O or CO_2 present in the remaining melt expressed as a whole system. The dashed area depicts the old concentration of H_2O or CO_2 in the liquid from the previous iteration step $\left(C_L^O\right)$.

2.1. Fractional Crystallization

At the beginning of the simulation, the melt fraction (F) is 1. At each iteration step, the melt fraction is reduced by a pre-defined increment (e.g., $\Delta F = 0.01$, Figure 1). The respective new melt fraction of the whole system (F^N) is calculated by multiplying the old melt fraction (F^O) with $1 - \Delta F$:

$$F^N = F^O(1 - \Delta F) \tag{1}$$

The simulation ceases if F^N reaches a lower threshold value, which is set to 0.01 (1% melt left). Since the exact threshold value terminating a crystallization process is unknown, we varied this threshold value and found that the influence on the results is negligible (see Supporting Information S1). To compute the ongoing crystallization, we apply the equation of fractional crystallization (e.g., Gast, 1968; Shaw, 1970):

$$C_L = C_0 F^{D-1} \tag{2}$$

where C_L is the concentration of a specific element or molecule (here H_2O or CO_2) in the liquid and C_0 is the initial concentration of this element or molecule in the system. D is the partition coefficient between the melt and the mafic minerals of a certain element or molecule. Based on literature values, the partition coefficient of H_2O $\left(D_{H_2O}\right)$ is assumed to be 0.01 (Dixon et al., 1988; P. Michael, 1995; P. J. Michael, 1988) and that of CO_2 $\left(D_{CO_2}\right)$ 0.001 (e.g., Rosenthal et al., 2015; Workman & Hart, 2005, for detail see Supporting Information S1).

It should be noted that during crystallization the content and solubility of the volatiles change, as does temperature, density and melt fraction. Since there is a strong feedback between the decreasing melt fraction and the temperature, the solubility and the density (leading potentially to a rise of melt during the crystallization or exsolution of volatiles), it is not possible to solve Equations 1 and 2 as such. Instead, we need to discretize the crystallization to take the changing conditions into account. In our calculation, F is replaced by $1 - \Delta F$ in Equation 2. This is because we assume that the melt is directly separated from the precipitated crystals. At each iteration step, C_L must be considered as a new, separated system $\left(C_L^N\right)$ that is entirely molten (Figure 1). Hence, the local old melt fraction of the liquid system from the previous step $\left(F_L^O\right)$ is always 1 and the local new melt fraction of the liquid system of the current step $\left(F_L^N\right)$ is $1 - \Delta F$. The modified equation to calculate the current amount of H_2O or CO_2 in the liquid for each iteration step is therefore:

$$C_L^N = C_L^O(1 - \Delta F)^{D-1} \tag{3}$$

C_L^O is the concentration of H_2O or CO_2 in the liquid from the preceding iteration step.

2.2. Temperature Calculation

The pressure is a fixed parameter in our calculations, which we chose depending on the depth of the hypothetical intrusion (unless buoyancy of melt is considered, see Section 2.4). In contrast, the temperature is decreasing within a molten body, causing crystallization and therefore lowering the melt fraction. For this reason, at each iteration step we calculate the temperature for a specific pressure. We do this by parameterizing the hydrated solidus and liquidus line for basalt of Mysen and Richet (2018) with the experimental data from Lambert and Wyllie (1972). The resulting best fit polynomial to calculate the liquidus temperature (T_{liq}) and the solidus temperature (T_{sol}) is valid over the pressure range of 0.2–3.4 GPa.

$$T_{sol} = -43.037P^3 + 279P^2 - 495.81P + 1161.3 \tag{4}$$

$$T_{liq} = -9.6265P^3 + 69.821P^2 - 138.79P + 1446.6 \tag{5}$$

The lithostatic pressure (P) is in GPa and T_{sol} and T_{liq} are in K. The resulting temperature (T) of the system for the specific pressure and the current melt fraction (F^N) is calculated in K as well:

$$T = T_{sol} + F^N\,(T_{liq} - T_{sol}) \tag{6}$$

As already mentioned, the evolution of the major elements in the melt from a basaltic towards an andesitic composition (Grove & Kinzler, 1986) is not taken into account for simplicity. For this reason, the change in solidus and liquidus temperature with composition is also not considered. Nevertheless, we tested the possible effects of taking such a compositional change into account (see Section 4.1). For this purpose, we parameterized the hydrated solidus and liquidus line for a tonalitic composition of Stern et al. (1975). The parameterization is valid over the pressure range of 0.2–3 GPa.

$$T_{sol_t} = -22.526P^3 + 155.01P^2 - 270.69P + 1039.9 \tag{7}$$

$$T_{liq_t} = -6.8584P^3 + 75.09P^2 - 179.88P + 1330.9 \tag{8}$$

2.3. Solubility and Volatile Release

The solubility of the volatiles in the melt is obtained by applying the solubility law of Parfitt and Wilson (2008). The quantity of volatiles that can be dissolved in a basaltic melt (H_2O_{dis} and CO_{2dis}) is computed in wt.% and pressure is in MPa:

$$H_2O_{dis} = 0.1078P_{H_2O}^{0.7} \tag{9}$$

$$CO_{2dis} = 0.0023P_{CO_2} \tag{10}$$

The partial pressure of either H_2O or CO_2 (P_{H_2O} or P_{CO_2}) is computed iteratively from the lithostatic pressure (P). We apply the bisection method, a mathematical method of finding a solution by repeated subdivision into intervals. This is done to derive the correct value for P_{H_2O} and P_{CO_2} in the volatile phase in equilibrium with the melt. We assume that H_2O and CO_2 are the only species present in the gas phase. Therefore, the exsolution of H_2O and CO_2 is intrinsically coupled, even though the applied solubility laws have been derived for pure species (see Supporting Information S1 for a comparison of pure-species and mixed-species solubility laws).

Furthermore, we consider that the amount of dissolved volatiles does not exceed the actual amount of volatiles available in the system. If the melt volatile content exceeds the solubility threshold, volatile release occurs. In this case, the quantity of H_2O and CO_2 that can be dissolved in the melt is the new concentration of the respective volatile species in this melt (C_L^N).

2.4. Density of the Melt

Due to crystallization, the remaining melt is increasingly saturated with volatiles. This should have a considerable effect on the density of the melt. If the melt is less dense than the surrounding rock, buoyant rise should occur. Such an ascent would lead to a decline in pressure and thus solubility (e.g., Gaillard & Scaillet, 2014; Holloway, 1998; Holloway & Blank, 1994; Iacono-Marziano et al., 2012; Newman & Lowenstern, 2002; Papale, 1997, 1999; Parfitt & Wilson, 2008; Shinohara, 2008), which in turn influences the release of the volatiles. In this study, we investigate two scenarios: (a) In the first scenario, the density of the melt relative to the surrounding solid (and the potential buoyancy of the melt) is not considered, hence the pressure would remain constant while the melt is solidifying. (b) In the second scenario, the buoyancy of the melt is taken into account. We compute the density of the melt ρ_{L}, each crystallization step applying the equation of state (EOS) after Lesher and Spera (2015). For this melt density calculation, a melt composition is required. The melt composition used to calculate the density is that of a tholeiitic glass sample (sample 519 4-1 from Bryan and Moore (1977), which is listed in Table S1 of Supporting Information S1). The current amount of H_2O and CO_2 in the melt $\left(C_L^N\right)$ of each individual iteration step (after subtracting the amount released) is added to this melt composition which does not include H_2O and

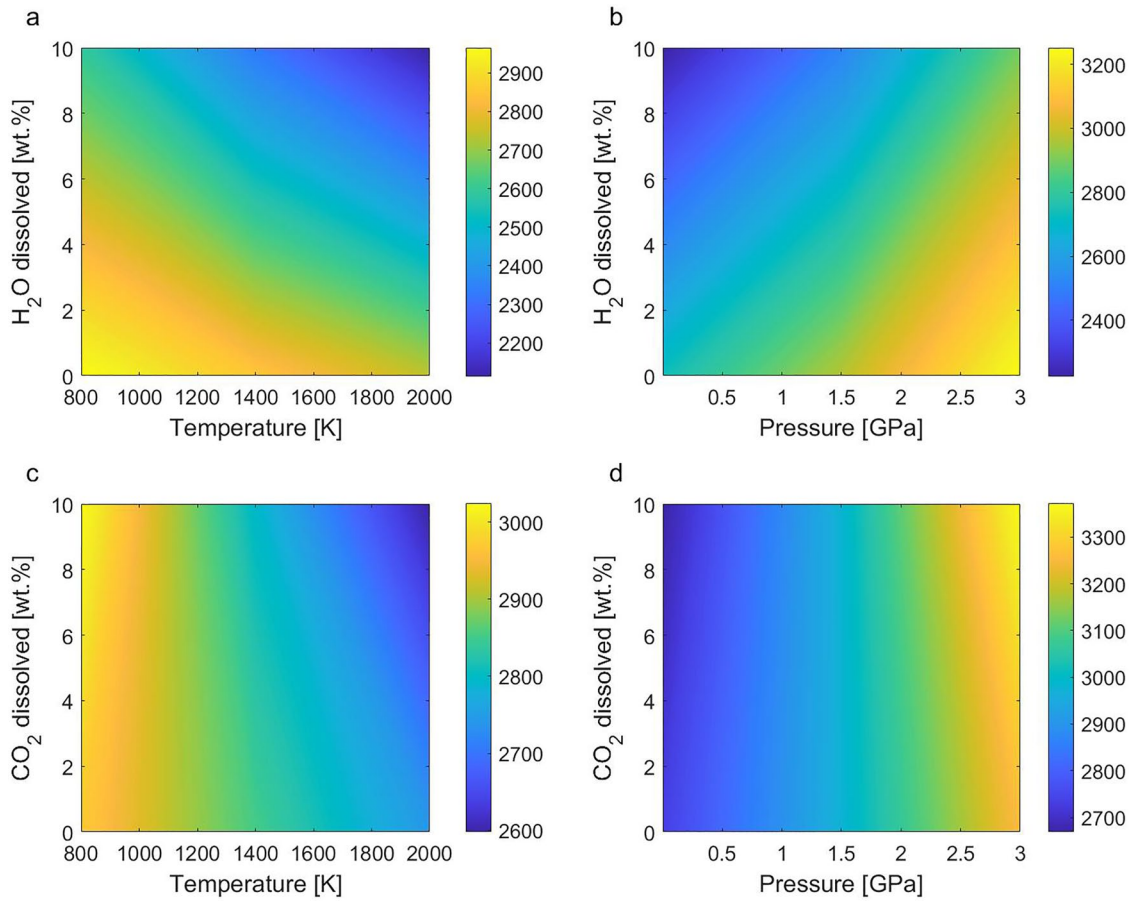

Figure 2. Variation of the melt density (color map in kg/m^3) as a function of (a and b) the H_2O and (c and d) the CO_2 content and the temperature or the pressure. In (a and b) the H_2O and in (c and d) the CO_2 content is set to zero, respectively. In (a and c) the pressure is 1 GPa and in (b and d) the temperature is 1200 K.

CO_2. We note again that the change of main components in the melt due to fractional crystallization is neglected for simplicity in this model. However, the effect of this process on the melt density is discussed in Section 4.2.

Figures 2a and 2b illustrate the considerable impact of water on the melt density. With increasing H_2O content and temperature, the melt density decreases significantly (Figure 2a). In contrast, the density of the melt is increasing as a function of pressure (Figure 2b). The influence of CO_2 on the melt density is shown in Figures 2c and 2d.

Subsequently, we compare the density of the evolving melt with the density of the surrounding rock. For the latter, we apply the Preliminary reference Earth model (PREM) of Dziewonski and Anderson (1981). The density transitions in the pressure range of interest (10^{-4} to 3 GPa) according to the PREM are at 0.38 GPa (bottom of upper crust) and at 0.65 GPa (bottom of lower crust). The density of the host rock is 2,600 kg/m^3 from the surface down to 0.38 GPa and 2,900 kg/m^3 from 0.38 to 0.65 GPa. If the density of the melt is larger than the density of the host rock, the melt is gravitationally stable, no ascent occurs and the calculation continues unchanged. In contrast, if the density of the remaining liquid is lower than the density of the solid rock, the melt ascends. For simplicity, we assume that exclusively the liquid phases are rising (melt and volatile phase) without any solid cumulates. In nature, however, it is likely that the melt crystallizes at least partially on its way up and may thus drag some crystals with it (see Discussion Section 4.2). Moreover, we expect the melt and the volatile phase to ascend separately, as it is anticipated for mafic melts (if the velocity of the volatile phase is higher than the velocity of the melt, Gonnermann & Manga, 2007). According to the density changes of the host rock (PREM), the melt either rises to the bottom of the upper crust (0.38 GPa), where it can intrude, or it directly ascends to the surface. In both cases, the temperature in K is adiabatically scaled up, from the pressure and the temperature

at depth (P_{down} and T_{down}, respectively) to the pressure and temperature of the upper crust (3.8×10^8 Pa) or the surface (10^5 Pa; P_{up} and T_{up}, respectively):

$$T_{up} = T_{down} \exp\left(\frac{-\alpha}{\rho_L Cp}\left(P_{down} - P_{up}\right)\right) \tag{11}$$

The density of the melt (ρ_L) is calculated using the EOS after Lesher and Spera (2015) as described above. The heat capacity of the melt (Cp) is calculated after Noack et al. (2016):

$$Cp = \Sigma \frac{Cp_{m,i} X_i}{X_i M_i} \tag{12}$$

where X_i is the mole fraction, $Cp_{m,i}$ is the molar heat capacity and M_i is the molar mass of the ith oxide component of the melt composition specified above. The values of $Cp_{m,i}$ ($\mathrm{J} \times \mathrm{K}^{-1} \times \mathrm{gfw}^{-1}$) are taken from Lesher and Spera (2015). The thermal expansion coefficient of the melt (α) is calculated after Lesher and Spera (2015) for a melt assemblage similar to the formula used in Noack et al. (2016):

$$\alpha = \sum X_i \left(\frac{\left(\frac{\delta V_i}{\delta T}\right)_P}{V_i} \frac{\rho_L}{\rho_i}\right) \tag{13}$$

X_i is the mole fraction, $\left(\frac{\delta V_i}{\delta T}\right)_P$ is the thermal expansion, V_i is the partial molar volume and ρ_i the density of the ith oxide component of the melt composition specified above. The values of $\left(\frac{\delta V_i}{\delta T}\right)_P$ and V_i are listed in, and ρ_i is calculated after Lesher and Spera (2015).

It should be noted at this point that intrusive and extrusive volatile release cannot always be completely separated from each other. We assume that the majority of extrusions were previously intrusive, since the melt probably partially emplaces within the crust before reaching the surface (thus they should be counted as intrusive-extrusive cases). In this study, we refer to any volatile release from a melt that has intruded within the lithosphere at some point as intrusive release. However, the intrusive-extrusive cases occur only for relatively high initial volatile contents (see Discussion Section 4.1). In our model, the melt is not ascending at a melt fraction of less than 0.07 ($F^N < 0.07$) even if it has a lower density than the surrounding rock. A melt fraction of 7% is suggested to indicate the melt-connectivity transition (Rosenberg & Handy, 2005). When crystallization has progressed to the point where the melt pockets are no longer connected, buoyant rise is not expected. Rosenberg and Handy (2005) assume that this melt-connectivity transition of 7% to be identical for melting and for crystallization. Therefore, we adopt a minimal melt fraction of 7% below which we consider an ascent of the remaining melt to be unlikely. Though, this value could potentially be lowered down to 2%–3% (Fraeman & Korenaga, 2010; Noack et al., 2012).

If the melt rises, there are three possible scenarios that can occur. (a) The adiabatically scaled up temperature of the melt (T_{up}) is higher than the liquidus temperature (T_{liq}) calculated for the specific pressure within the crust or at the surface (P_{up}). (b) T_{up} is between T_{liq} and T_{sol}. We assume here that in this case the melt fraction is 1 again, since only the melt (without crystals) is rising. Thus, the current temperature of the melt has to be calculated as in Equation 6, but by exchanging the melt fraction with a recalculated melt fraction for the new pressure. (c) T_{up} is lower than T_{sol}. In this case, the melt is not rising in our simulations but emplaces. This can be justified by the reasonable assumption that the melt would completely crystallize during its way up (otherwise the adiabatically calculated temperature of the melt would not be lower than the solidus temperature). Further, we assume that in scenario (c) the solidification would occur shortly after the melt begins to rise. Our assumption is based on several simulation runs under varying initial conditions. All of these runs reveal that the difference between the temperature of the melt and the solidus temperature prior to ascent is minor. Furthermore, this case only applies if we adopt a minimum melt fraction of 0.03 (instead of 0.07). We therefore assume that buoyancy is unlikely under these conditions, so we prevent the melt from rising by not adjusting the pressure and temperature condition in such a case.

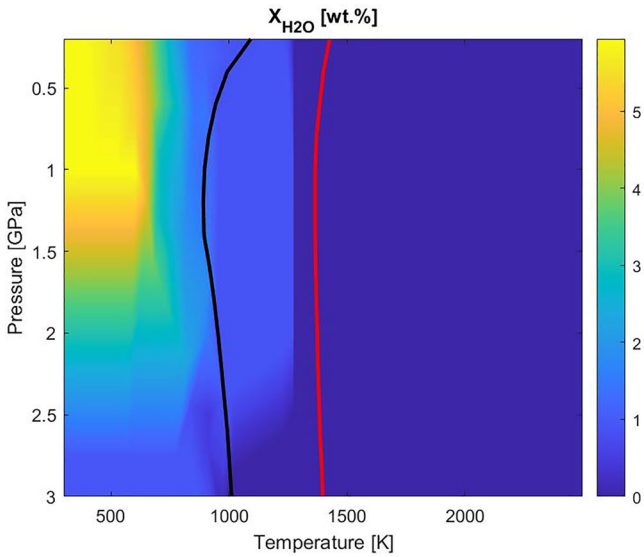

Figure 3. H_2O solubility [wt.%] in hydrous phases of a mid-ocean ridge basalt composition as a function of pressure and temperature. X_{H_2O} is the amount of H_2O that can be incorporated into the phase assemblage. The data is interpolated from the phase diagram of Iwamori (1998), Iwamori (2004, 2007), Nakagawa et al. (2015), and Nakagawa and Iwamori (2017). This diagram is based on the data from Schmidt and Poli (1998) and references therein. The black line indicates the solidus curve and the red line the liquidus curve of a hydrated basalt after Mysen and Richet (2018).

In addition, the hydrated solidus and liquidus temperatures (T_{sol} and T_{liq}) as well as the melt temperature are recalculated for the specific P_{up} by applying Equations 4–6. This can cause a numerical issue since we use the parameterization of the hydrated solidus and liquidus to calculate T_{sol} and T_{liq} as explained above. However, from 3 GPa upwards to lower pressures, the hydrated solidus curve first decreases to a minimum temperature of 887.69 K ($T_{\min}$) at 0.12 GPa before it rises again (Mysen & Richet, 2018). This can cause that the temperature calculated for the ascended melt is higher than the temperature calculated at depth. Since a temperature increase during buoyant ascent is unlikely, we set T_{sol} equal to $T_{\min}$ in such a case (T_{sol} = 887.69 K) to prevent model inconsistencies. This minimum solidus temperature is applied exclusively in the case of melt ascent from the crust to the surface (if the pressure is below 0.12 GPa). The reason for the high solidus temperatures near the surface is that generally less volatiles are present in the melt compared to greater depths. Since the solubility of H_2O and CO_2 decreases together with the pressure (e.g., Gaillard & Scaillet, 2014; Holloway, 1998; Holloway & Blank, 1994; Iacono-Marziano et al., 2012; Newman & Lowenstern, 2002; Papale, 1997, 1999; Parfitt & Wilson, 2008; Shinohara, 2008, see Section 3.1), less H_2O and CO_2 can be dissolved within the melt close to the surface, which leads to an increase of the solidus temperature (Dasgupta, 2018). However, this is only true for a system in equilibrium, which is probably not the case for an ascending melt. However, the fixation of T_{sol} to $T_{\min}$ also depresses the melt temperature, leading to a higher melt density and thus to a slightly delayed ascent.

2.5. Hydrous and C-Bearing Minerals

Depending on the pressure and temperature conditions, hydrous phases (e.g., amphiboles) are able to incorporate certain quantities of OH. In the context of intrusions, such minerals could either precipitate directly from the melt during fractional crystallization or they might form when the volatile phase separates from the melt and reacts with the surrounding mantle. We consider this effect in our simulations by interpolating the data given by Iwamori (1998), Iwamori (2004, 2007), Nakagawa et al. (2015), and Nakagawa and Iwamori (2017) for the pressure and temperature range of interest (Figure 3). This diagram comprises the solubility of H_2O in hydrous minerals as a function of pressure and temperature for a mid-ocean ridge basalt composition with the data from Schmidt and Poli (1998) and references therein. However, it is important to keep in mind that not all of the phases indicated in Figure 3 can crystallize from a basaltic melt because of the high basaltic solidus temperature (Schmidt & Poli, 1998). To trace the possible crystallization range in our model, we have added the parameterized solidus and liquidus from Equation 4 and 5 in the figure.

A MATLAB function is used to return the amount of H_2O that can be incorporated into the phase assemblage of a basaltic rock $\left(C_{S_{hyd}}\right)$ under the distinct pressure and temperature conditions. Therefore, $C_{S_{hyd}}$ is the maximal amount of H_2O consumed by both, hydrous as well as nominally anhydrous minerals. If we take the formation of hydrous minerals into account, for each iteration step, a different way of calculating C_L^N must be applied. So far, the current H_2O content of the melt (C_L^N, which is needed to calculate the solubility of volatiles) was obtained by applying the equation of fractional crystallization (Equation 3). Since the partition coefficient (D) exclusively accounts for the amount of a certain element or molecule (in this case H_2O or CO_2) that can be incorporated by nominally anhydrous minerals (such as olivine and pyroxene), D is not sufficient to account for the amount of H_2O that can be incorporated into hydrous minerals. Depending on the pressure and temperature conditions, significantly more water partitions into the solid when hydrous phases are formed. According to our model, hydrous minerals crystallizing from a basaltic melt can contain up to 1.2 wt.% H_2O until the solidus is reached (Figure 3). For comparison, nominally anhydrous minerals, stable in a basaltic melt can only incorporate about 0.1–0.15 wt.% H_2O (Aubaud et al., 2004; Hauri et al., 2006). Thus, the redistribution

of H_2O between solid and liquid is now no longer calculated via D but via the maximum water capacity of the crystals $\left(C_{S_{hyd}}\right)$.

At first, it is necessary to compute X_S and X_L. These variables represent the volume-dependent amount of H_2O or CO_2 in the solid or liquid, respectively, expressed as a whole system. The quantity of H_2O in the volume-dependent solid system of the current step $\left(X_S^N\right)$ is required to obtain the current H_2O content of the melt $\left(C_L^N\right)$. X_S^N is calculated by adding the concentration of H_2O in the solid that is currently crystallizing $\left(C_{S_{hyd}}\right)$ to the sum of the amount of H_2O from the previous iteration steps $\left(C_S^O\right)$. The volume dependence is established by multiplying the respective amount of H_2O in the solid (from the current and previous iteration steps) with the regarding melt fraction. This melt fraction is the difference between F^O and F^N for $C_{S_{hyd}}$ and $1 - F^O$ for C_S^O (Figure 1).

$$X_S^N = C_{S_{hyd}}\left(F^O - F^N\right) + C_S^O\left(1 - F^O\right) \tag{14}$$

The H_2O concentration of the currently crystallizing solid phases $\left(C_S^N\right)$ is calculated by dividing X_S^N by the difference between the initial melt fraction (Equation 1) and the current melt fraction (F^N).

$$C_S^N = \frac{X_S^N}{1 - F^N} \tag{15}$$

To obtain the current amount of H_2O in the liquid phase $\left(C_L^N\right)$, the quantity of H_2O in the current total, volume-dependent liquid $\left(X_L^N\right)$ has to be calculated:

$$X_L^N = C_0 - X_S^N - H_2O_{rel}^{tot} \tag{16}$$

C_0 is the initial concentration of H_2O here (as we examine the incorporation into hydrous phases) from the beginning of the calculation. If we subtract X_S^N from this initial value, we obtain X_L^N. If release occurred in the previous iteration steps, the released volatiles are not part of the system anymore. Thus, the sum of H_2O released so far $\left(H_2O_{rel}^{tot}\right)$ has to be subtracted from the initial concentration as well.

The current H_2O content of the melt $\left(C_L^N\right)$ is obtained by dividing X_L^N by F^N (Figure 1). Subsequently, the solubility is calculated by applying Equations 9 and 10.

In our study, we do not consider the formation of C-bearing minerals. The reason for this is that carbonate minerals are not thought to be stable at a pressure lower than ~2 GPa (Brey et al., 1983; Dasgupta, 2018; Falloon & Green, 1989; Yaxley et al., 2019). At lower pressures, only nominally carbon-free phases are expected to precipitate, and it is assumed that the amount of CO_2 that can be incorporated into these phases is insignificant (Dasgupta, 2018; Keppler et al., 2003; Shcheka et al., 2006). In our study, the effect of nominally carbon-free minerals is covered by the partition coefficient of CO_2 between the melt and the solid rock. At higher pressures (above 2 GPa), previous studies suggest that about 10 wt.% carbonates (like dolomite or magnesite) are stable in a basaltic rock composition (Dasgupta et al., 2004; Hammouda, 2003; Kiseeva et al., 2013). The measured CO_2 content of these minerals is approximately 50 wt.% (Dasgupta et al., 2004; Kiseeva et al., 2013). However, since experiments always represent closed systems, CO_2 is unable to partition into a volatile phase and rise, so it must be squeezed into carbonate minerals. In contrast, we expect under natural conditions a volatile phase (including H_2O and CO_2) to form at pressures lower than 2 GPa instead of carbonate minerals. This volatile phase may ascend due to its own overpressure or by already existing cracks or fissures (as mentioned above). Hence, we neglect the formation of C-bearing minerals in this study.

In addition, during melting processes under oxidizing conditions CO_2 is substantially partitioning into the melt (Holloway, 1981; Holloway et al., 1992; Ortenzi et al., 2020). It can therefore be assumed that under these conditions CO_2 is not incorporated into the solid either (at least not to a higher quantity as already considered by the partition coefficient). The upper mantle is presumably oxidized since the early Archean (e.g., Canil, 1997; Delano, 2001; Li & Lee, 2004; Scaillet & Gaillard, 2011; Trail et al., 2011), and thus the effect of C-bearing phases on the volatile release can be neglected. However, constraining the exact quantity of CO_2 that can be exsolved from mafic intrusions would require a detailed phase diagram of the CO_2 solubility in a basaltic phase assemblage as a function of pressure and temperature (as available for H_2O). Unfortunately, there is not enough data available from experiments (especially at higher pressures) for the construction of such a phase diagram, which also takes into account oxygen fugacity and the possibility of a gas phase rising. Furthermore, a detailed

calculation of the melt ascent including the volume of the melt, temperature decrease and accompanying crystallization as a function of time would be required.

3. Results

To examine the influence of the different processes described in Section 2, we first run the simulations without taking into account the density of the melt and the formation of hydrous phases. Subsequently, we compare these findings with the results of the simulations considering these processes to gain a better understanding of their significance.

If not described differently, for all figures the following fixed input parameters are used: The pressure is set to 1 GPa, the partition coefficient of H_2O to 0.01 and for CO_2 to 0.001. For the initial volatile content of the melt three different cases are investigated: Case 1 with initially 0.05 wt.%, Case 2 with initially 0.5 wt.% and Case 3 with initially 2 wt.% H_2O and CO_2, respectively. We chose 0.05 wt.% as lower limit according to the lowest content of H_2O in (depleted) basaltic magmas (e.g., Gaillard & Scaillet, 2014; Gaillard et al., 2021; Helo et al., 2011; Saal et al., 2002). However, for most figures 0.1 wt.% is used as lower limit since 0.05 wt.% is hardly visible. As an upper limit, we adopted 2 wt.% with respect to the upper H_2O content of ocean island basalts (OIBs, e.g., Gaillard et al., 2021, and references therein). The value of 0.5 wt.% is chosen as an intermediate value. To facilitate the comparison for the release of the volatile species, we set the CO_2 content equal to the respective H_2O value. These values agree well with the literature. The minimum amounts of CO_2 in a (depleted) basaltic magma start at ∼0.02 wt.% (Saal et al., 2002) and the maximum amounts may even go beyond the values applied in our study, as high as 5 wt.% (e.g., Gaillard et al., 2021, and references therein). For all initial volatile contents, the temperature varies from 1368 K at the onset to 892 K at the end of the crystallization process.

3.1. Simplified Model Without Density and Hydrous Phases

To constrain the amount of H_2O and CO_2 that can be dissolved within a basaltic melt and to benchmark our simulation, we successfully reproduced Figure 3 of Gaillard and Scaillet (2014) apart from sulfur (which is neglected in our study; Figure 4a). The temperature is a fixed value of 1573.15 K (1300°C) and the pressure ranges from 10^{-6}–10^{3} bar (10^{-10}–10^{-1} GPa) as in Gaillard and Scaillet (2014). The solubility calculation of Iacono-Marziano et al. (2012) is applied (see Supporting Information S1), which considers the bulk rock composition of an alkali basalt from Mt. Etna (sample ETN-1 from Lesne et al. (2011b) and Iacono-Marziano et al. (2012); see Table S1 in Supporting Information S1). In addition, we display the amount of H_2O and CO_2 that can be released from the melt for comparison. In Figure 4a, the solubility of the two volatile species increases considerably as a function of pressure and thus the volatile exsolution decreases. At 1,000 bar, H_2O and CO_2 are almost entirely dissolved within the melt, meaning that almost no release can take place. Moreover, the solubility of CO_2 is considerably lower compared to that of H_2O, which is in agreement with the literature (e.g., Holloway, 1976; Holloway & Blank, 1994; Parfitt & Wilson, 2008; Shinohara, 2008). The difference in solubility of the two volatile species varies with pressure. As can be seen in Figure 4a, at 10 bar the solubility of CO_2 is about 95% lower compared to H_2O and at both, 0.01 and 1,000 bar about 10%–15%. In Figure 4b, we show the same simulation but taking into account fractional crystallization (from F = 1 to F = 0.01). Due to fractional crystallization, the amount of H_2O and CO_2 that can be released is significantly enhanced, resulting in a substantial reduction of volatiles dissolved in the melt. This particularly applies for higher pressures.

The role of fractional crystallization, enhancing the volatile saturation of the liquid and thus triggering the release of H_2O and CO_2 is illustrated in Figure 5. The hypothetical intrusion simulated in this figure is emplaced within the lithospheric mantle at 1 GPa. At this pressure level, the solubility of H_2O and CO_2 is so high that all H_2O and CO_2 is dissolved within the melt (Figure 4). Therefore, neither H_2O nor CO_2 can be released from the magma body at the onset of the crystallization process (Figure 5a). Due to ongoing crystallization and associated volatile accumulation in the remaining melt (Figure 5b), the solubility is exceeded at a certain threshold and the volatile release initiates (Figure 5a). The melt fraction at which this threshold is reached increases as a function of the

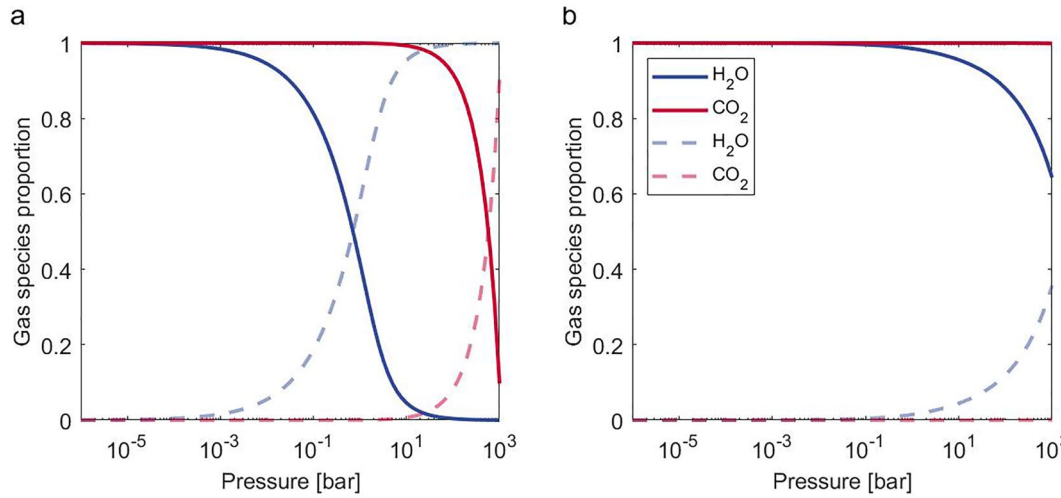

Figure 4. Proportion of H_2O and CO_2 released (solid lines) and dissolved (dashed lines) as a function of pressure. (a) Without fractional crystallization considered and (b) with fractional crystallization implemented in the calculation. Dashed lines in (a) are reproduced from Gaillard and Scaillet (2014). The initial content of H_2O and CO_2 is 0.1 and 0.06 wt.%, respectively. The temperature is a constant value of 1573.15 K.

initial H_2O and CO_2 content. This is due to the fact that the saturation of the melt is reached more rapidly if more volatiles are initially present. At 2 wt.% H_2O and CO_2, for example, the exsolution initiates almost from the beginning, whereas at 0.05 wt.% the release is delayed until the melt is saturated due to accumulation. Owing to the reduced solubility of CO_2 relative to H_2O (Figure 4a), CO_2 is the first phase being released from the melt. However, as soon as one species is exsolved from the melt, the other volatiles present are released simultaneously

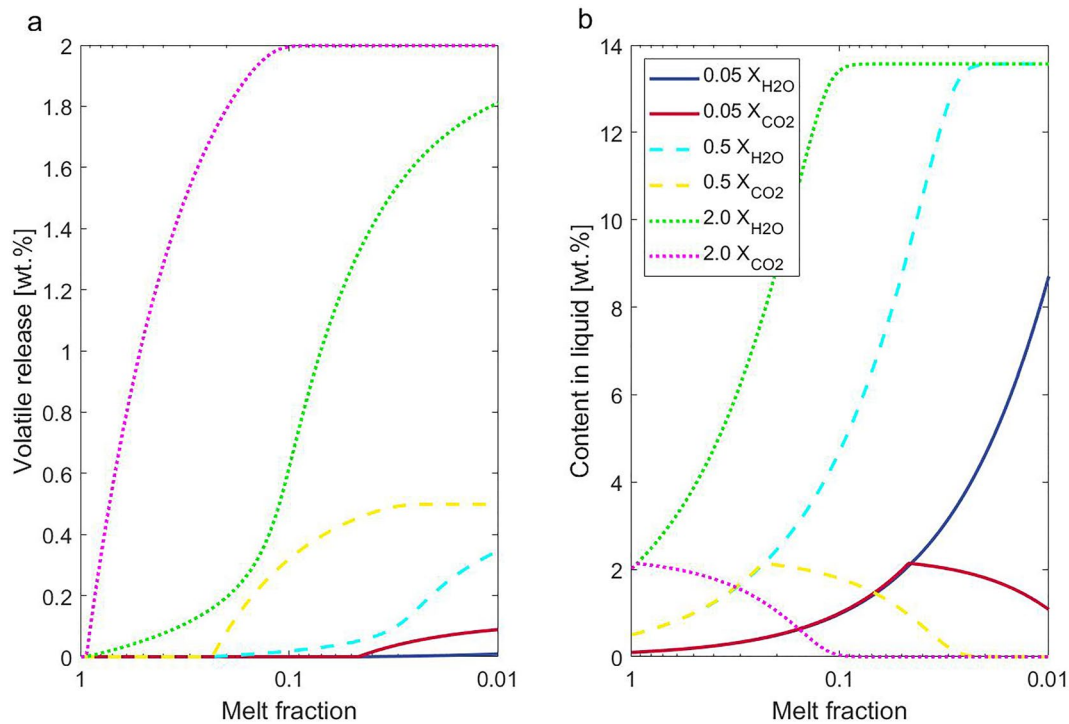

Figure 5. H_2O and CO_2 (a) released from the melt and (b) dissolved within the melt as a function of the melt fraction. The individual line types are specified in the legend and represent the three different cases for H_2O and CO_2. Case 1 starts with initially 0.05 wt.%, Case 2 with initially 0.5 wt.% and Case 3 with initially 2 wt.% H_2O and CO_2, respectively.

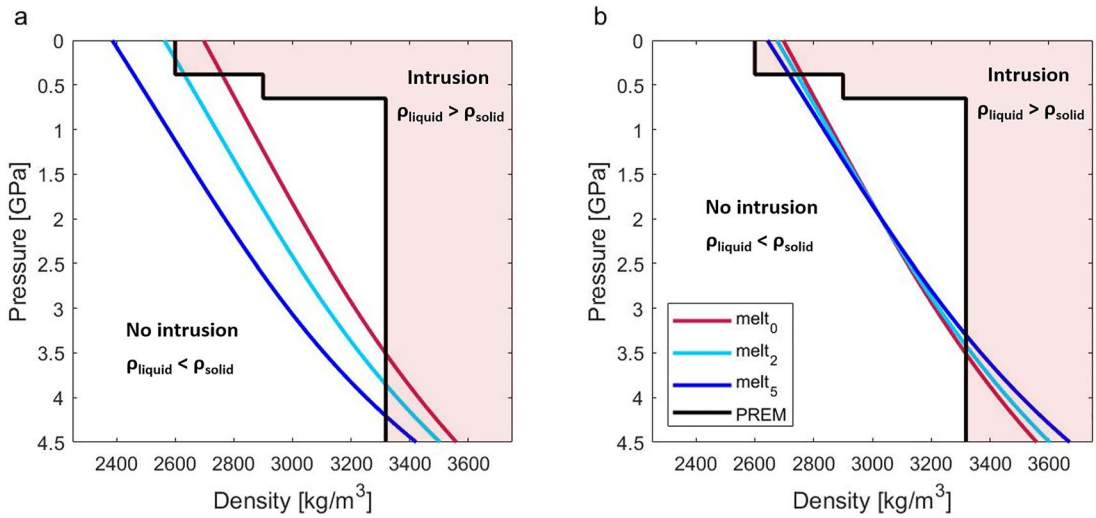

Figure 6. Density of the melt (colored lines) and the solid host rock (black lines) as a function of the pressure. The subscripts in the legend indicate the initial amount of (a) H_2O and (b) CO_2 in the melt in wt.%. The density of the host rock is calculated using the PREM (see Section 2). In the PREM, the upper crust reaches a depth of 15 km (~0.38 GPa) and the lower crust of 24 km (~0.64 GPa). The reddish area marks the part of the lithosphere where the density of the melt is higher compared to the density of the host rock and thus intrusions are likely according to our model. In the white area, no intrusions are expected.

to a limited extent (Parfitt & Wilson, 2008, Figure 5a). The reason for this is the chemical equilibrium between the melt and the arising volatile phase. The solubility of the volatiles is dependent on their partial pressures. If no H_2O is present, the partial pressure of H_2O is zero in the newly formed volatile phase, and thus the melt and the volatile phase are not in equilibrium. In order to change this, some H_2O is partitioning into the volatile phase. Therefore, even though H_2O alone would remain dissolved in the melt a minor proportion of H_2O is taken along into the gas phase due to the release of CO_2 (Parfitt & Wilson, 2008). In our model, this process is reflected by the iterative algorithm used to find the gases in equilibrium with the melt (see Methods Section 2.3). For this reason, H_2O is exsolved together with CO_2 even if its solubility is not yet exceeded. However, CO_2 is released to a higher proportion than H_2O. Likewise, this can be attributed to the distinct solubility of the two volatile species. In general, the more H_2O and CO_2 are initially in the melt, the more can be released. The abrupt termination of the CO_2 accumulation in Figure 5b appears once the melt saturation for CO_2 is reached and the release has initiated. The latter results in a gradual depletion of CO_2 in the liquid phase until nothing is left (Figure 5b), since all CO_2 is released (Figure 5a). As mentioned above, at the beginning of the crystallization process the solubility of water is not yet exceeded, and thus only a small amount is exsolved due to the release of CO_2. Hence, the H_2O content in the liquid continues to increase until the solubility of H_2O is exceeded, resulting in a strong release of H_2O (Figure 5b).

3.2. Influence of Density and Hydrous Phases

The accumulation of volatiles in the melt illustrated in Figure 5b leads to a decrease in the melt density. We calculated this melt density as a function of pressure and compared it to the density of the host rock (Figure 6). In Figure 6a the H_2O content and in Figure 6b the CO_2 content of the melt is varied from 0 to 5 wt.% (the content of the respective other species is set to zero). The melt density declines considerably with increasing H_2O content (Figures 2a, 2b and 6a).

If the density of the host rock exceeds the density of the melt, the melt is rising. This is the case for a pressure range from about 3.5 (or 3.8 GPa depending on the H_2O content) to 0.38 GPa for a melt with 0 to ~2.5 wt.% H_2O and from about 4.2 GPa to the surface for a melt with H_2O concentrations greater than ~2.5 wt.% (Figure 6a). Instead, if the density of the host rock is lower compared to the melt density, the melt intrudes. This is the case for pressures greater than 3.5 GPa as well as for pressures less than 0.38 GPa. The latter only applies for melts with H_2O concentrations below ~2.5 wt.% (Figure 6a). The effect of the initial CO_2 content of the melt is less

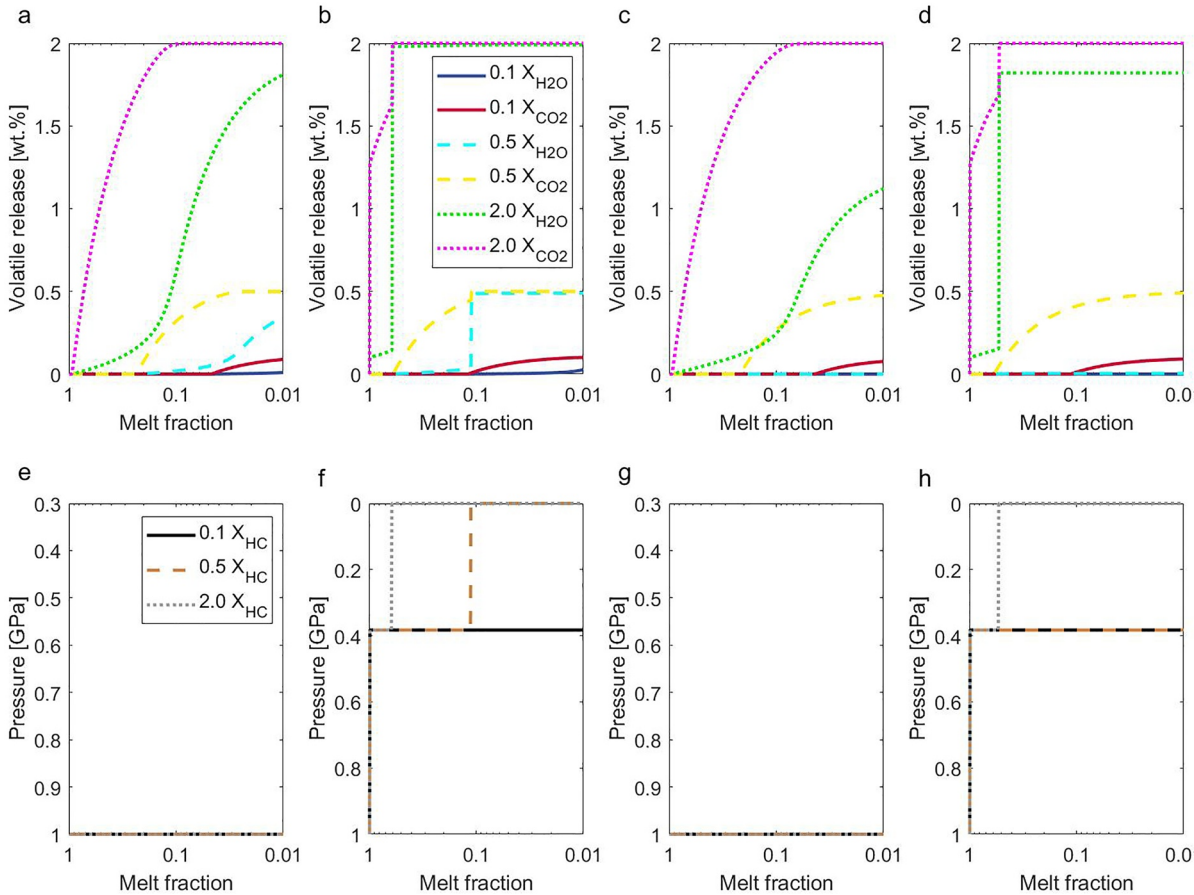

Figure 7. (a–d) Comparison of the quantity of H_2O and CO_2 that can be released and (e–h) the associated pressure that acts on the melt as a function of the melt fraction. (a and e) Neither the density of the melt nor the formation of hydrous phases is considered. (b and f) The density is considered but not the formation of hydrous phases. (c and g) The formation of hydrous minerals is included but not the density. (d and h) The density as well as the formation of hydrous minerals is considered. Fractional crystallization is considered in all diagrams. The different line types and colors in (a–d) are the same as shown in Figure 5. They indicate the three cases with different initial volatile contents (Case 1: 0.1 wt.%, Case 2: 0.5 wt.%, Case 3: 2 wt.% H_2O and CO_2). We used 0.1 wt.% as lower limit here (instead of 0.05 wt.%) to ensure that the release curves are still visible. (e–h) The respective pressure line of Case 1–3 is specified in the legend. The starting value of the pressure is 1 GPa for all diagrams. The *y*-axis of (e–h) is varied for better visibility of pressure changes during crystallization.

pronounced (Figure 6b), which is in agreement with the literature (Sakamaki et al., 2013). The density of the host rock exceeds the density of the melt for each initial value of CO_2 from about 3 to 0.38 GPa.

Applying the melt density calculation to our magma body crystallization simulation has almost no influence on the final CO_2 release since all CO_2 was exsolved already before considering the buoyancy of the melt (Figures 7a and 7b). Only in Case 1 (initially 0.1 wt.% H_2O and CO_2, respectively), a few ppm more CO_2 are exsolved in the end, if the density consideration is included. In contrast, the elevation of the total H_2O exsolution is (Figure 7b). While in Case 1, the total amount of released H_2O is slightly enhanced, H_2O is entirely exsolved in Case 2 and 3 (initially 0.5 and 2.0 wt.% H_2O and CO_2, respectively). Moreover, the initiation of the volatile release takes place at a higher melt fraction if the density is considered. In Case 3, this even leads to a direct release of H_2O and CO_2. Due to the lower density of the melt compared to the host rock at 1 GPa (Figure 6, white area), the melt immediately ascends to the upper crust (0.38 GPa). Since the water content of the melt at the beginning of the crystallization process is below 2.5 wt.%, the melt intrudes instead of rising directly to the surface. This accounts for all three initial volatile contents (0.1, 0.5, 2 wt.% H_2O and CO_2, respectively). At 0.38 GPa (bottom of upper crust) less volatiles can be dissolved within the melt compared to higher pressures. As a consequence, the release of H_2O and CO_2 is already possible at a higher melt fraction. Due to the early exsolution, more volatiles can be released in total compared to the simulation where the density is not taken into account (Figure 7a). In Case 1 the

initial volatile content of 0.1 wt.% H_2O and CO_2 is so low, that the melt is not rising further to the surface. Instead, in Case 2 and 3 (0.5 and 2.0 wt.% H_2O and CO_2) the initial volatile content is relatively high from the beginning on. For this reason, in combination with the accumulation of volatiles during crystallization at 0.38 GPa, the melt becomes less dense than the host rock again and rises to the surface. At surface pressure, however, the solubility is sufficiently low to immediately release the entire remaining volatiles (Figure 7b). As a consequence, in Case 2 and 3 the exsolution curves of H_2O and CO_2 overlap for those cases, as both species are depleted. A step wise shape of the release curve for H_2O in Case 2 and for both, H_2O and CO_2 in Case 3 is noticeable. This is caused by the implementation of the buoyant ascent in our model, namely the immediate rise of the melt from 1 to 0.38 GPa and (depending on the initial volatile content) from 0.38 GPa to the surface.

If the formation of hydrous minerals is implemented in the calculations (but not the density) the H_2O release does not occur at all in Case 1 and 2 (initially 0.1 and 0.5 wt.% H_2O and CO_2, respectively), while it is significantly reduced in Case 3 (initially 2.0 wt.% H_2O and CO_2, respectively; Figure 7c). If hydrous phases precipitate from the melt, they can include huge amounts of H_2O (Figure 3). Hence, for relatively low and intermediate initial H_2O contents of the melt (as in Case 1 and 2), all H_2O is incorporated into the hydrous minerals, so nothing can be exsolved. For rather high initial H_2O concentrations (as in Case 3) about 50% of the H_2O partitions into the hydrous phases, while the rest can still be released. The exsolution of CO_2 is not influenced, since CO_2 is not incorporated into hydrous minerals. The melt fraction, at which the volatile release initiates, is the same as in Figure 7a as the effect of the melt ascent and the associated reduction of the solubility is not taken into account here.

Combining all processes (fractional crystallization, melt density, and formation of hydrous phases), the effect on the release of CO_2 is minor (Figure 7d). Only for Case 1, the amount of CO_2 that is released at the end of the crystallization process is slightly elevated compared to Figures 7a and 7c, where the density is not considered. On the contrary, the release of H_2O is completely suppressed in Case 1 and 2 due to the formation of hydrous minerals. In Case 3, compared to Figures 7a and 7c, the final amount of H_2O that can be released is elevated, whereas it is diminished in comparison to Figure 7b. While the increase is due to the buoyancy of the melt, the reduction can be attributed to the formation of hydrous phases.

As described in Section 2, the lithostatic pressure is a fixed value as long as we exclude the density. This is the case for Figures 7e and 7g, where the initial value of the pressure is 1 GPa and the density is not taken into account. In these scenarios, the melt crystallizes at this pressure level without rising. On the contrary, in Figures 7f and 7h the density contrast between the melt and the solid rock is considered. The simulation starts at a pressure of 1 GPa as well, however, the melt is directly rising to 0.38 GPa. At this upper crustal pressure, the melt emplaces for initial volatile contents of 0.1 wt.% (Figures 7f and 7h) and 0.5 wt.% (Figure 7h). For 0.5 and 2 wt.% H_2O and CO_2, respectively, in Figure 7f and for 2 wt.% H_2O and CO_2 in Figure 7h, the melt rises again at a certain melt fraction until the surface pressure (10^{-4} GPa) is reached.

3.3. Variation of the Pressure

To examine the effect of the pressure on the volatile release, we run simulations for 0.01, 0.1, 2, and 3 GPa (Figure 8). This is done for all three cases with the initial volatile contents of 0.1, 0.5, and 2 wt.% by including the buoyancy effect as well as the formation of hydrous minerals. A pressure variation without considering the buoyancy effect and the formation of hydrous minerals is shown in Supporting Information S1. The effect of the pressure variation on the final release of H_2O is noticeable but not crucial, while the release of CO_2 is not affected at all (Figures 8a–8d). In general, the higher the pressure, the less volatiles can be released due to the increasing solubility. However, this effect is attenuated on the one hand due to the process of fractional crystallization (leading to an enhanced accumulation of volatiles and thus to the exceedance of the saturation limit) and on the other hand due to the effect of buoyant rise at pressures higher than 0.38 GPa. In contrast, the formation of hydrous minerals consumes H_2O, leading to a reduced exsolution.

At 0.01 GPa (~0.3 km depth), the pressure and thus the solubility of the volatiles are so low that the volatile release initiates from the beginning on (Figure 8a). The complete exsolution of H_2O is, however, prevented due to its higher solubility compared to CO_2 in combination with the formation and OH-incorporation of hydrous

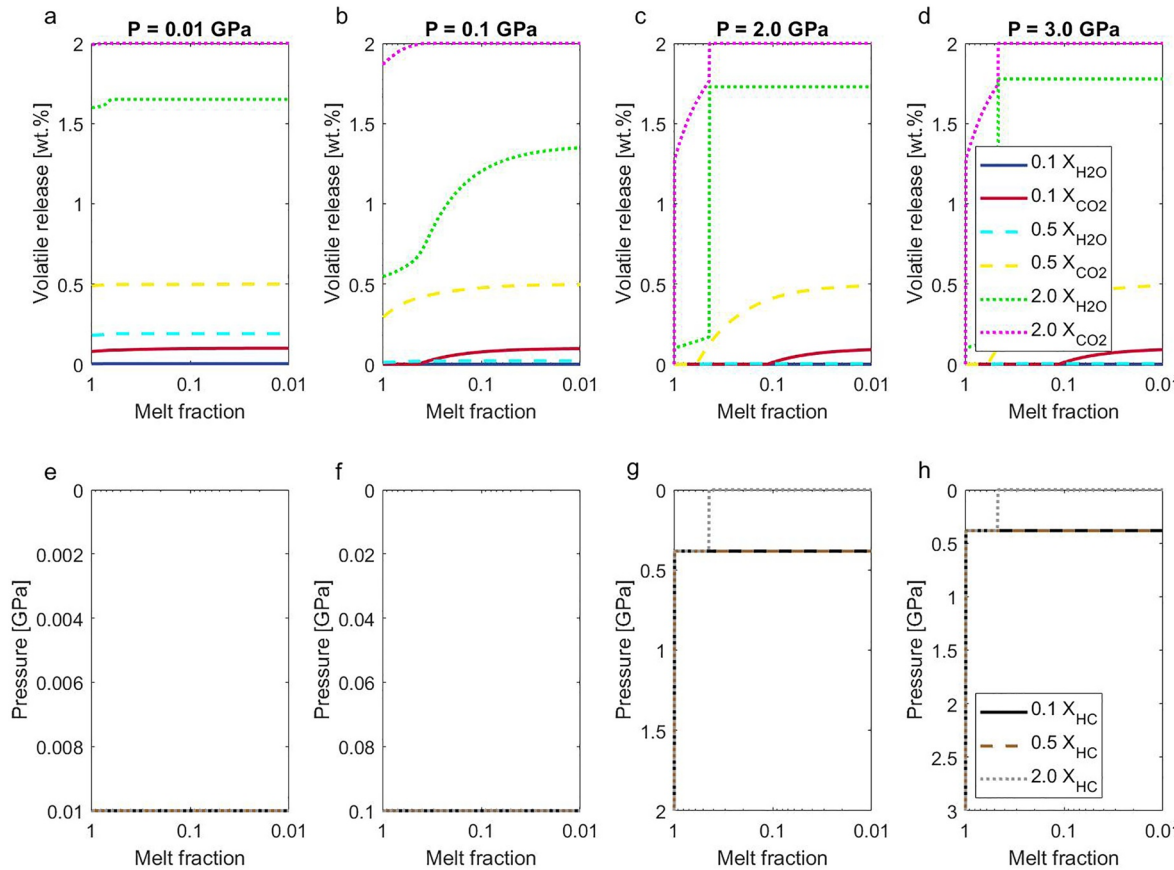

Figure 8. (a–d) H_2O and CO_2 released from the melt and (e–h) the pressure that acts on the melt as a function of the melt fraction for different initial pressures. The initial pressure in (a and e) is 0.01 GPa, in (b and f) is 0.1 GPa, in (c and g) is 2 GPa and in (d and h) is 3 GPa. The *y*-axis has different scales for the pressure for better visibility of pressure changes during crystallization. The different line types and colors are the same as shown in Figures 5 and 7. They indicate the different initial volatile contents (Case 1: 0.1 wt.%, Case 2: 0.5 wt.%, Case 3: 2 wt.% H_2O and CO_2) as explained in the text and specified in the legend. The calculation of the melt density and the formation of hydrous minerals is included in this figure.

phases. At 0.1 GPa (~3.3 km depth) immediate volatile exsolution occurs only for rather high initial volatile contents (Case 2 and 3) and the final H_2O exsolution is reduced for all Cases (Figure 8b). This is caused by the relatively elevated solubility of H_2O and CO_2 due to the increased pressure.

At 2 and 3 GPa (~66.7 and 100 km, respectively), the volatile release is even more delayed due to the higher solubility of the volatiles at these pressures (Figures 8c and 8d). In general, the volatile release pattern is similar as at 1 GPa (Figure 7d), because in all these simulations the melt rises directly to 0.38 GPa (Figures 7h, 8g and 8h). The reason for this is the lower density of the melt compared to the density of the host rock in this pressure range (Figure 6). In contrast to Figures 8a and 8b, starting at 0.01 and 0.1 GPa, the solubility at 0.38 GPa is higher, and thus less volatiles are released immediately from the melt. This, in combination with the high initial volatile content in Case 3, causes the melt to rise once again and to reach the surface (Figures 8g and 8h). Consequently, almost the entire volatile budget of the melt is released except for 0.2 to 0.3 wt.% H_2O (at 3 and 2 GPa, respectively), which is incorporated into hydrous phases (Figure 8c and 8d).

The associated pressure that acts on the melt is shown in Figures 8e–8h. For an initial pressure of 0.01 and 0.1 GPa, the pressure remains constant for all 3 cases as no buoyant rise takes place. On the contrary, for initially 2 and 3 GPa, the melt rises directly to the upper crust (0.38 GPa), and subsequently to the surface for Case 3 (Figures 8g and 8h).

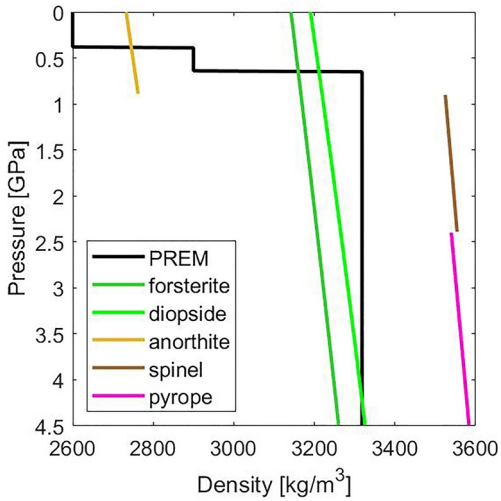

Figure 9. Comparison of the solid rock density according to the PREM with the density of common mantle minerals. The colors representing the minerals are given in the legend. The aluminum phase minerals are only displayed within the pressure range in which they occur.

4. Discussion

4.1. Melt Ascent and the Effect of the Density

By calculating and comparing the density of the melt with the density of the host rock, we obtain that for a large part of the uppermost mantle intrusions are not anticipated (Figure 6). According to our calculations, basaltic melts with H_2O contents of 0–2.5 wt.% are only expected to be gravitationally stable at pressures higher than ~3.5 (around the lithosphere-asthenosphere boundary) and lower than 0.38 GPa (bottom of upper crust). If the melt has high H_2O contents (more than ~2.5 wt.%), it will probably not even intrude within the upper crust (~0.38 GPa), but will ascend directly to the surface (Figure 6a).

However, these findings and exact threshold values should be taken with caution, as they are mainly determined by the low density of the upper crust predicted by the PREM (2,600 kg/m^3 from 0.38 GPa upwards). Moreover, the density of the crust and the uppermost mantle (up to ~24.4 km) are constant values, which are averaged over the entire globe. Nevertheless, the PREM is a reasonable representation of the density profile of the Earth's lithosphere even though it is a simplified model. In Figure 9 the density of the endmembers of typical mantle minerals is added for reference. These mineral densieties are calculated using an equation of state from Stixrude and Lithgow-Bertelloni (2011).

While forsterite and diopside (dominant phases) are present within the entire lithosphere, plagioclase, spinel and pyrope (aluminum phase) are plotted only for the pressure range in which they occur (Winter, 2014). The figure illustrates that the density of the host rock within the upper mantle calculated according to the PREM corresponds to the density of the major upper mantle minerals. However, the composition of the crust is very heterogeneous, which means that a comparison of the density of the crust by mineral composition is not straightforward.

Dziewonski and Anderson (1981) used an average weight for the first 100 km, assuming that the oceanic crust constitutes 2/3 of the surface of the Earth. This implies that 1/3 is supposed to be the continental crust. In general, the crust is less dense compared to the mantle and the continental crust is less dense than the oceanic crust. Since we only simulate intrusions within the oceanic lithosphere, the density of the crust calculated with the PREM is probably slightly underestimated. This assumption is in agreement with more recent studies estimating the density structure of the oceanic lithosphere (Afonso et al., 2007; Hynes, 2005; Lee et al., 2005). In these models, the density of the crust ranges from approximately 2,900 to 3,475 kg/m^3 depending on the depth as well as on the age of the oceanic lithosphere. The higher density of the oceanic crust proposed in these studies, compared to the density of the melt calculated here, implies that generally no emplacement should occur within the oceanic crust. Since the density of the continental crust is significantly lower compared to the oceanic crust, intrusions within the continental crust are more likely. Nevertheless, intrusions at the bottom as well as within the crust are common features observed in seismic profiles (e.g., Galland et al., 2018; Menand, 2011, and references therein) and field studies of ophiolites (Galland et al., 2018). The main reason for the emplacement, at a low or even insufficient density contrast between the melt and the host rock, is the difference in rigidity and rheology at the bottom and within the crust. It is assumed that several intrusions are caused by this change in material or rheological behavior of the rocks (Galland et al., 2018; Menand, 2011). To model these material differences within the crust is beyond the scope of this study. However, we assume that the emplacement within the crust is a common feature, and the simplest way to simulate this is to use the sharp threshold of the PREM (from 2,600 to 2,900 kg/m^3 at ~0.38 GPa, Figure 6). An even more pronounced change in density, material behavior and rheology occurs at the lithosphere-asthenosphere boundary. This chemical and thermal boundary layer acts as a barrier for the ascending melt. Therefore, intrusions are most likely and seismically indicated at this depth level (e.g., Afonso et al., 2007; Green et al., 2010; Hynes, 2005; Lee et al., 2005; Sakamaki et al., 2013), which is in agreement with Figure 6. According to this figure, intrusions are supposed to occur at depths of about 3.5 GPa or higher (depending on the initial H_2O content of the melt).

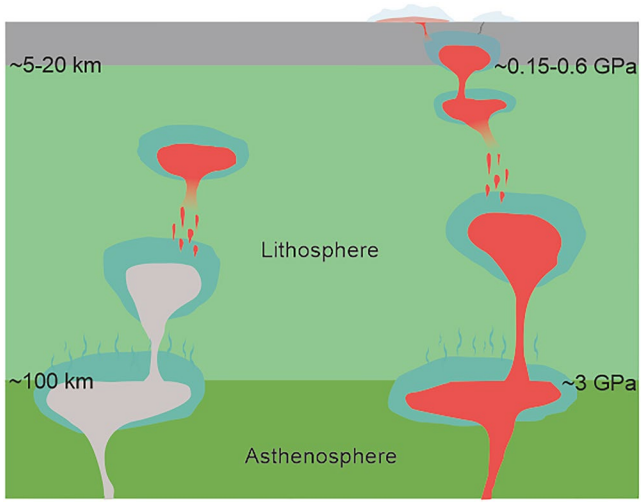

Figure 10. Sketch of intrusions within or directly beneath the lithosphere (not to scale). The mixing cascades indicated here display possibilities for volatiles to reach the surface even if they are released rather deep and react with the mantle to form hydrous phases. Gray parts reveal intrusions, which have crystallized completely, red parts indicate molten magma bodies and light blue parts represent the hydration of the surrounding rock and the ascent of supercritical liquids.

The results displayed in Figure 7b demonstrate that the effect of adopting the PREM instead of a higher density for the oceanic crust after Hynes (2005), Lee et al. (2005), and Afonso et al. (2007) is minor and only slightly influences melts with low volatile contents. If we would omit the PREM and would use higher density values, the density contrast between the solid rock and the melt would be insufficient for the melt to intrude within the crust. In this case, the melt would directly ascend to the surface and release its entire volatile budget. However, by applying the PREM, complete exsolution of the volatiles occurs in Case 2 and 3 anyway. Thus, for melts with initial H_2O and CO_2 concentrations of 0.5 wt.% or greater the uncertainties regarding the density of the crust are negligible. The only difference is that the complete volatile release is slightly delayed using the PREM. However, the results would differ in Case 1. For a melt with originally 0.1 wt.% H_2O and CO_2, the release of H_2O is suppressed using the PREM while for a higher density of the crust, the melt would rise to the surface and release all volatiles. However, as already discussed, other factors like changes in the rheology and material properties cause intrusions independent of the density and render an emplacement within the crust as most likely.

The abrupt ascent of the melt to the crust and/or the surface (Figures 7b and 7d) is an artifact of the way this ascent is implemented in our simulation by using the density threshold values of the PREM. A melt that originates within the lithosphere, is modeled to either directly reach the crust or surface depending on the H_2O content (Figure 6). This is done by setting the pressure immediately to 0.38 GPa for the upper crust or to 10^{-4} GPa for the surface, if the density of the melt is lower than that of the host rock. This simplification is the reason for the stepped shape of the H_2O and CO_2 release curves (Figures 7b and 7f for Case 2 and 3 and in Figures 7d and 7h, Figures 8c, 8d, 8g and 8h, and Figure 9 for Case 3). In reality, the shape of these curves is presumably smooth. In principle, it can be assumed that the melt crystallizes due to the adiabatic temperature drop and may even solidify. Indeed, an ascent from the lower part of the lithosphere or perhaps even from the lithosphere-asthenosphere boundary all the way up to the surface or crust may not be feasible owing to the rapid solidification of the melt (Cruden & Weinberg, 2018). As described in the Methods section, for simplicity we assume that the melt rises without any crystals. However, even if the crystals sink quickly, in nature there might probably be some which are dragged up with the melt or the crystals form during the ascent. Whether a melt that intrudes deep within the lithosphere can reach crustal or surface levels or crystallizes on its way up depends on several factors apart from the density such as the volume of the melt, the composition and the temperature of the melt and the mantle, the rheology of the mantle as well as the velocity of the melt ascent (e.g., Cruden & Weinberg, 2018). To examine if and how the melt rises within the lithosphere in greater detail is beyond the scope of this study.

Even if the melt is not able to rise all the way up to the crust, a deep-released volatile phase could ascent through pre-existing fissures or by its own overpressure. At high pressures and temperatures, supercritical liquids form instead of a gas phase, leading to immiscibilities between the melt and the exsolved liquid phase (e.g., Ballhaus et al., 2015; Murphy et al., 2021). During the ascent, these liquids likely react with the surrounding mantle to form hydrated mineral phases (like amphibole, phlogopite or phengite). If these hydrated parts of the lithospheric mantle melt again, the volatile-rich magma will rise and either hydrate the mantle (or the crust) further up or it will directly contribute to an extrusive system. Hence, via mixing cascades, even volatiles released deep within the lithosphere or bound within hydrous phases can finally reach the surface (Figure 10). Evidence for this mechanism is provided by the geological record, which reveals that large parts of the lithospheric mantle are metasomatized (e.g., Van Kranendonk et al., 2018).

An alternative possibility is that the liquids are replaced by anhydrous silicate phases, leaving behind pseudomorphs of the former fluid globules (e.g., Ballhaus et al., 2015; Murphy et al., 2021), while the fluid itself rises further up. However, this process as well as the fate of the volatiles is not well understood yet.

The viscosity is another important factor controlling the melt ascent. A low viscosity facilitates upward migration. However, the effect of the density appears to be more pronounced. For example, if the density is high while the viscosity is low, the melt does not rise despite the low viscosity (Sakamaki et al., 2013). In our study, we refrain from calculating the viscosity as we expect it to remain low during the crystallization process. This is because our calculations start with rather wet melts (0.01–2 wt.% H_2O), which accumulate even more H_2O and CO_2 due to crystallization. The viscosity decreases significantly as a function of the water content and therefore, it can be assumed that the viscosity of these wet melts is rather low. In addition, basaltic melts commonly display a lower viscosity in contrast to felsic compositions. However, due to crystallization even a basaltic melt should evolve at a certain point toward a more felsic composition. Since this evolution is neglected in our model, the increasing viscosity is neglected as well. Such an increase could theoretically prevent buoyancy. This assumption is supported by studies reporting a transition to a high viscosity mush below melt fractions of 50% (Costa et al., 2009). However, these studies require a homogeneous mixing of the melt and the crystals. Since we assume fractional crystallization to be the dominant mechanism in our model, a homogeneous mixing is not expected.

Furthermore, in our simulations the melt ascends directly after starting the simulation (at $F = 0.99$) to the bottom of the upper crust (e.g., Figures 7b, 7d, 8c and 8d). Thus, the effect of crystallization on the viscosity (and on the ascent) can be excluded for this first rise to the crust. However, it could play a role for the second rise in our simulations from 0.38 GPa to the surface. On the other hand, the density of the melt is dramatically reduced if the composition is rather silicic, which in turn favors the buoyant rise considerably. The solidus and liquids temperature is reduced for felsic relative to mafic compositions (Stern et al., 1975), however, this only has a weak influence on the density of the melt. Another consequence of fractional crystallization is the early removal of dense minerals like olivine and pyroxene. This again leads to a decrease of the density (Sparks & Huppert, 1984), favoring buoyant rise. If the effects discussed above would lead to a lower melt density, this would also influence the maximum water content of the melt (2.5 wt.%), at which intrusions at the bottom of the upper crust (0.38 GPa) can occur according to the PREM (see Section 3.3). Therefore, this value has to be taken with caution.

Since all the processes discussed have opposite effects on the buoyancy of the melt, calculating the exact conditions under which melt ascent occurs is complex. However, intrusions within the crust are observed and highly likely. Where exactly these intrusions occur can vary and is not well constrained. The ascent of melt to the surface is not in question, as it is expressed by extrusive volcanism all over the world. We suggest that these extrusive eruptions mostly originate from melts that do not rise directly to the surface after melting, but first intrude (perhaps even several times), partially crystallize, and then continue to rise. The consequence is that a majority of extrusive eruptions may originate from previously intrusive melts. These more complex pathways to extrusive melts (influencing e.g., estimates on volcanic outgassing fluxes) are, however, not yet considered in modeling studies. Especially the volatile content and speciation may strongly differ in intrusive-extrusive melts compared to melts that directly rise to the surface without fractional crystallization.

To get an idea of the sensitivity of our model, we run several simulations with different initial conditions (not shown). We tested the effect on the results in case the melt would not be able to ascend all the way up to the surface, but would (finally) emplace within the crust. In the first scenario, the melt intrudes at 0.38 GPa (preventing the buoyant rise) and in the second scenario, the melt ascends close to the surface and emplaces at 0.15 GPa (~5 km depth, e.g., Petraske et al., 1978; Planke et al., 2005). In addition, we run all these simulations for an andesitic melt composition (Table S1 in Supporting Information S1) with adapted solidus and liquidus temperatures. We found that for both scenarios, the only difference to a melt that is allowed to rise to the surface is that only 70% H_2O for a purely basaltic and 50% for an andesitic composition can be released in Case 3 (initially 2 wt.%) instead of 85%–90% as in Figures 7d, 8c and 8d. The reason for this is that in Case 1 and 2 H_2O is completely incorporated into hydrous minerals and CO_2 is entirely released for all cases anyway. These results are also valid if we assume an intensive increase in viscosity at a melt fraction of 0.5, which prevents the melt from buoyancy. Thus, the uncertainty in considering the surface rise is 15%–20% for the release of H_2O for a purely basaltic and about 45%–50% for an andesitic composition (for rather high initial volatile contents).

Altogether, our findings suggest that the buoyancy consideration has an impact on the final volatile release, especially on H_2O. The magnitude of this impact depends on the initial volatile concentration, the local density, rheology and material properties as well as the composition of the melt and the surrounding rock.

Table 1
Quantity of H_2O That Can Be Released in Percent for Different Starting Pressures (Without Considering the Buoyancy and the Formation of Hydrous Minerals)

	Case 1	Case 2	Case 3
0.01 GPa	3%	40%	85%
0.1 GPa	0%	5%	70%
1 GPa	0%	0%	85%
3 GPa	0%	0%	90%

Note. The initial volatile contents are 0.1 wt.% (Case 1), 0.5 wt.% (Case 2), and 2 wt.% (Case 3). These values are the results of simulations without including the processes of buoyant ascent and the formation of hydrous minerals (see Figure S1 Supporting Information S1).

4.2. Volatile Release Within the Lithosphere

As we want to investigate the likelihood of the volatile release from magmatic intrusions within the whole lithosphere, the depth of the emplacement and therefore the lithostatic pressure is an important parameter. Including all processes (the effect of fractional crystallization, the melt density calculation and the formation of hydrous phases), the influence of the pressure on the volatile release is visible (Figures 8a–8c), but less pronounced than predicted when considering exclusively the solubility (e.g., Gaillard & Scaillet, 2014; Iacono-Marziano et al., 2012; Parfitt & Wilson, 2008). We find that the variation of the pressure between the lithosphere-asthenosphere boundary and the crust is of minor relevance since the effect of the melt buoyancy at pressures higher than 0.38 GPa dominates. Within the upper crust (< 0.38 GPa) the release of H_2O varies considerably as a function of pressure, while the amount of CO_2 that can be released is unaffected.

To quantify the volatile release at different pressures, we display the amount of H_2O that can be released in percent for all Cases (0.1, 0.5 and 2.0 wt.% H_2O and CO_2, respectively) in Tables 1 and 2. The amount of CO_2 that can be released is not shown as it is always 100%. However, if the density and the formation of hydrous phases are not taken into account, there are two exceptions for the CO_2 release in Case 1 (see Figure 1 in Supporting Information S1): at 1 GPa only about 90% and at 3 GPa only about 45% CO_2 can be released. The numbers in Tables 1 and 2 should be taken with caution, as they depend on several parameters discussed in this study, most of which are not well constrained. A variation of other input parameters, such as the temperature, the initial melt composition and the partition coefficient can be found in Supporting Information S1.

4.3. Comparison With Extrusive Outgassing and Implications for Early Earth

It is proposed that the intrusive contribution to the total magma production on Earth is around 80% for oceanic (and around 90% for continental) settings (Crisp, 1984; Lourenço et al., 2020). However, assuming that most of the extrusive magmatism was intrusive at one point, this number would even be higher. Our study suggests, that from these 80% almost all CO_2 and 0%–85% H_2O can be released (Figures 7d and 8). The latter strongly depends on the initial volatile content, buoyancy and the associated lithostatic pressure as well as the precipitation of hydrous phases. Most of these parameters are only poorly constrained and require further investigation. Moreover, it is not clear which quantity of volatiles released from deep intrusions (between the lithosphere-asthenosphere boundary and the crust) can finally reach the surface (see Section 4.2).

As mentioned earlier, most previous models estimating the fluxes of volatiles or the composition of an early atmosphere overlook the intrusive release of volatiles. Combined with the predominance of intrusive magmatism, this means that the release of volatiles on the early Earth is probably underestimated. If we assume, for example, that a melt with initially 2 wt.% H_2O and CO_2 originates at 1 GPa, then according to our model about 100% CO_2 and 85% H_2O can be released from this melt. In contrast, from a melt that originates at the same pressure but with a low initial volatile content (0.1 wt.% H_2O and CO_2), still about 100% CO_2 but 0% H_2O can be released (Figure 7d). These values apply for a simulation including the buoyancy of the melt and the formation of hydrous minerals. As an example, we can assume, that from the (at least) 80% of intrusive magmatism on early Earth, 50% of the released volatiles can actually reach the surface (this is just an example assumption since the quantity of volatiles released from an intrusion which can reach the surface is not constrained). In this case, the release of CO_2 would be enhanced by a factor of 2 and H_2O by a factor of 0–1.8 (considering intrusive systems) than what has been assumed so far exclusively for extrusive systems. The increase of the total CO_2 release of a factor of 2 considering intrusive volatile release is consistent with the findings of Hartley et al. (2014).

Table 2
Quantity of H_2O That Can Be Released in Percent for Different Starting Pressures (With Considering the Buoyancy and the Formation of Hydrous Minerals)

	Case 1	Case 2	Case 3
0.01 GPa	90%	100%	100%
0.1 GPa	70%	90%	95%
1 GPa	10%	70%	90%
3 GPa	5%	40%	80%

Note. The initial volatile contents are 0.1 wt.% (Case 1), 0.5 wt.% (Case 2), and 2 wt.% (Case 3). These values are the results of simulations including the processes of buoyant ascent and the formation of hydrous minerals.

To benchmark our results, we can compare them to field observations and volatile phases in melt inclusions. Gas bubbles trapped in melt inclusion are often used to recalculate the initial volatile content of the melt (e.g., Moore et al., 2015; Nava et al., 2021; Rosenthal et al., 2015). Moore et al. (2015) stated that only gas bubbles that were formed after entrapment should be used to estimate the volatile concentration of the melt and the trapping pressures. However, such bubbles could have been trapped after a certain degree of crystallization, and thus volatile accumulation had taken place in the melt. This in turn, would lead to an overestimation of the initial volatile content in the melt. In contrast, if degassing already occurred, the analysis of the bubbles would underestimate the initial volatile content (Hartley et al., 2014; Petrelli et al., 2018; Rosenthal et al., 2015). Our model results strongly suggest, that intense degassing of the melt occurs especially for CO_2 (e.g., Figures 7–9). A release of nearly all CO_2 in our model (∼100%) is consistent with a CO_2 release of 90% at crustal depths (Wallace, 2018). The lower the pressure and the higher the initial volatile content, the more volatiles (even H_2O) are released from the melt (see Tables 1 and 2). The literature values for an estimated intrusive CO_2 release are with at least 40%–60% (Hartley et al., 2014; Nava et al., 2021) lower than our results since we assume a CO_2 release of about 100%. However, on the one hand, we do not consider the formation of C-bearing phases so far, which could lead to a reduction of the CO_2 release. On the other hand, the CO_2 content in the gas bubbles could be underestimated due to degassing prior to entrapment as discussed above. This assumption is reasonable because of the low solubility of CO_2 and the rather low entrapment pressure of 0.1–0.2 GPa (Hartley et al., 2014; Nava et al., 2021). Moreover, for a precise comparison, we would need to know the exact initial volatile content of the melt, the pressure and temperature as well as the melt fraction of entrapment. These parameters are still not well enough constrained, making it challenging to compare our results to these measurements. For the H_2O release, our results partly overlap with the results of Parmigiani et al. (2017). They suggest in their study that more than 40%–50% of the initial H_2O content of the magma body should be released (for a pressure of 0.2 GPa and an initial H_2O content of the melt of 5.5 wt.%). They point out, that for this assumption, exclusively the process of the magmatic volatile phase transport by the formation of channels is considered, which is only investigated for a crystal fraction of 0.4–0.7. Further, Parmigiani et al. (2017) argue that a majority of the remaining volatiles has to be released by other mechanisms like ductile veining (Weinberg & Regenauer-Lieb, 2010) or capillary fracturing (Holtzman et al., 2012; Oppenheimer et al., 2015), since most of the plutonic rocks contain a H_2O content of less than 1 wt.% (Caricchi & Blundy, 2015; Parmigiani et al., 2014). Therefore, it can be assumed that the total volatile release is likely to be much higher than suggested by Parmigiani et al. (2017) if the whole crystallization process is considered.

Not only for early Earth but also for estimates of modern volatile fluxes, intrusive release is often neglected (e.g., Burton et al., 2013; Lee & Lackey, 2015). In general, our model could be used to improve constraints on modern volatile fluxes. However, the model would need to be adjusted. For example, a distinction would need to be made between oceanic and continental lithosphere and their different properties (e.g., composition, density, thickness, solidus and liquidus temperature). Without these modifications, it is difficult to provide a valid assumption. However, it can be assumed that the behavior of CO_2 should not change dramatically according to our model results since it is rather consistent with the lithosphere. Even at 3 GPa and without considering the buoyancy, 40%–100% of the initial CO_2 content (depending on the initial content in the melt) can still be released. Based on this assumption, modern CO_2 fluxes should also be about 1.5–2 times higher than without considering intrusive volatile release. Because the release of H_2O is highly variable (Tables 1 and 2), a simple estimate is not possible. However, these values should be investigated in more detail in future studies.

5. Conclusion

In this study, we present a novel numerical model to quantify the amount of H_2O and CO_2 released from mafic intrusions. For this purpose, the solubility of the volatiles, the process of fractional crystallization, the melt buoyancy, and the formation of hydrous minerals are taken into account. The main conclusion is that considering the intrusive volatile release, especially including the process of fractional crystallization has a strong influence on the total outgassing. By implementing the process of fractional crystallization, the volatile exsolution is generally possible within the whole lithosphere and the quantity of volatiles that can be released from intrusions increases significantly. However, intrusive release strongly depends on key factors like the initial volatile content (and thus the mantle volatile budget), the formation of hydrous minerals as well as the buoyancy of the melt. We found that the buoyancy and the formation of hydrous phases are essential factors influencing the (H_2O) release from magmatic intrusions. While the melt buoyancy favors the release of the volatiles, the partitioning of H_2O into

hydrous phases exclusively diminishes or even prevents the H_2O exsolution. Whether the H_2O release is suppressed again strongly depends on the initial volatile content and the lithostatic pressure (depth of emplacement). However, in this study, the melt is gravitationally unstable for a pressure range of 0.38 to ~3.5 GPa. If a melt originates within this pressure range it is supposed to rise directly to the bottom of the upper crust (~0.38 GPa). Therefore, the pressure only has a noticeable effect on the volatile exsolution at pressures lower than 0.38 GPa.

The dominance of intrusive magmatism on Earth renders the intrusive volatile release an essential factor determining the volatile fluxes and the composition of the early atmosphere. Since previous modeling studies constrained these mechanisms by exclusively considering extrusive outgassing, we propose that the volatile release on early Earth is underestimated. According to our study, the total outgassing should be enhanced by about 100% CO_2 and 0%–85% H_2O when including the contribution from intrusions within the lithosphere. In the future, it would be important to investigate the influence of C-bearing minerals on the CO_2 release as well as the effect of the oxygen fugacity on the total volatile release. In particular, the oxidation state in combination with the varying emplacement of intrusions could significantly influence the speciation of the volatiles. Our results suggest that intrusive volatile release is an important process in the atmospheric evolution of terrestrial bodies. This, in turn, is a crucial parameter for the habitability of Earth and other planets.

Data Availability Statement

Data arrays and the associated MATLAB scripts to reproduce our figures are stored in the TRR170-DB (Late Accretion Onto Terrestrial Planets) repository: https://doi.org/10.35003/MDMAJD (CC0—"Public Domain Dedication"). Figures and data were generated with MATLAB version R2020b: https://de.mathworks.com/products/. To download MATLAB a license is needed. However, the scripts and arrays can be executed using GNU Octave as well.

Acknowledgments
We would like to thank two anonymous reviewers as well as the editor Marie Edmonds for their constructive and helpful comments to improve the manuscript. The data for the water solubility as function of pressure and temperature of a basaltic rock composition was provided by Takashi Nakagawa who edited the original data from Hikaru Iwamori. We would like to thank Elis Hoffmann for the constructive discussion about early Earth conditions and hydrated veins in the mantle as well as Fabrice Gaillard for the discussion about solubility laws. This study was supported and funded by the Deutsche Forschungsgemeinschaft (DFG) within the SPP 1833 "Building a Habitable Earth," project number NO 1324/2-1. Open Access funding enabled and organized by Projekt DEAL.

References

Afonso, J. C., Ranalli, G., & Fernàndez, M. (2007). Density structure and buoyancy of the oceanic lithosphere revisited. *Geophysical Research Letters*, *34*(10), L10302. https://doi.org/10.1029/2007gl029515

Aubaud, C., Hauri, E. H., & Hirschmann, M. M. (2004). Hydrogen partition coefficients between nominally anhydrous minerals and basaltic melts. *Geophysical Research Letters*, *31*(20), L20611. https://doi.org/10.1029/2004gl021341

Ballhaus, C., Fonseca, R. O., Münker, C., Kirchenbaur, M., & Zirner, A. (2015). Spheroidal textures in igneous rocks – Textural consequences of H_2O saturation in basaltic melts. *Geochimica et Cosmochimica Acta*, *167*, 241–252. https://doi.org/10.1016/j.gca.2015.07.029

Brey, G., Brice, W., Ellis, D., Green, D., Harris, K., & Ryabchikov, I. (1983). Pyroxene-carbonate reactions in the upper mantle. *Earth and Planetary Science Letters*, *62*(1), 63–74. https://doi.org/10.1016/0012-821x(83)90071-7

Bryan, W., & Moore, J. G. (1977). Compositional variations of young basalts in the Mid-Atlantic Ridge rift valley near lat 36°49′N. *The Geological Society of America Bulletin*, *88*(4), 556–570. https://doi.org/10.1130/0016-7606(1977)88<556:cvoybi>2.0.co;2

Burton, M. R., Sawyer, G. M., & Granieri, D. (2013). Deep carbon emissions from volcanoes. *Reviews in Mineralogy and Geochemistry*, *75*(1), 323–354. https://doi.org/10.2138/rmg.2013.75.11

Canil, D. (1997). Vanadium partitioning and the oxidation state of Archaean komatiite magmas. *Nature*, *389*(6653), 842–845. https://doi.org/10.1038/39860

Caricchi, L., & Blundy, J. (2015). Experimental petrology of monotonous intermediate magmas. *Geological Society, London, Special Publications*, *422*(1), 105–130. https://doi.org/10.1144/sp422.9

Costa, A., Caricchi, L., & Bagdassarov, N. (2009). A model for the rheology of particle-bearing suspensions and partially molten rocks. *Geochemistry, Geophysics, Geosystems*, *10*(3). https://doi.org/10.1029/2008gc002138

Crisp, J. A. (1984). Rates of magma emplacement and volcanic output. *Journal of Volcanology and Geothermal Research*, *20*(3–4), 177–211. https://doi.org/10.1016/0377-0273(84)90039-8

Cruden, A., & Weinberg, R. (2018). Mechanisms of magma transport and storage in the lower and middle crust—Magma segregation, ascent and emplacement. *Volcanic and igneous plumbing systems*, 13–53. https://doi.org/10.1016/b978-0-12-809749-6.00002-9

Dasgupta, R. (2018). Volatile-bearing partial melts beneath oceans and continents—Where, how much, and of what compositions? *American Journal of Science*, *318*(1), 141–165. https://doi.org/10.2475/01.2018.06

Dasgupta, R., Hirschmann, M. M., & Withers, A. C. (2004). Deep global cycling of carbon constrained by the solidus of anhydrous, carbonated eclogite under upper mantle conditions. *Earth and Planetary Science Letters*, *227*(1–2), 73–85. https://doi.org/10.1016/j.epsl.2004.08.004

Degruyter, W., Parmigiani, A., Huber, C., & Bachmann, O. (2019). How do volatiles escape their shallow magmatic hearth? *Philosophical Transactions of the Royal Society A*, *377*(2139), 20180017. https://doi.org/10.1098/rsta.2018.0017

Delano, J. W. (2001). Redox history of the Earth's interior since ~3900 Ma: Implications for prebiotic molecules. *Origins of Life and Evolution of the Biosphere*, *31*(4), 311–341. https://doi.org/10.1023/a:1011895600380

Dixon, J. E., Stolper, E., & Delaney, J. R. (1988). Infrared spectroscopic measurements of CO_2 and H_2O in Juan de Fuca Ridge basaltic glasses. *Earth and Planetary Science Letters*, *90*(1), 87–104. https://doi.org/10.1016/0012-821x(88)90114-8

Dorn, C., Noack, L., & Rozel, A. (2018). Outgassing on stagnant-lid super-Earths. *Astronomy & Astrophysics*, *614*, A18. https://doi.org/10.1051/0004-6361/201731513

Dziewonski, A. M., & Anderson, D. L. (1981). Preliminary reference Earth model. *Physics of the Earth and Planetary Interiors*, *25*(4), 297–356. https://doi.org/10.1016/0031-9201(81)90046-7

Edmonds, M., Liu, E. J., & Cashman, K. V. (2022). Open-vent volcanoes fuelled by depth-integrated magma degassing. *Bulletin of Volcanology*, *84*(3). https://doi.org/10.1007/s00445-021-01522-8

Falloon, T. J., & Green, D. H. (1989). The solidus of carbonated, fertile peridotite. *Earth and Planetary Science Letters*, *94*(3–4), 364–370. https://doi.org/10.1016/0012-821x(89)90153-2

Fraeman, A. A., & Korenaga, J. (2010). The influence of mantle melting on the evolution of Mars. *Icarus*, *210*(1), 43–57. https://doi.org/10.1016/j.icarus.2010.06.030

Gaillard, F., Bouhifd, M. A., Füri, E., Malavergne, V., Marrocchi, Y., Noack, L., et al. (2021). The diverse planetary ingassing/outgassing paths produced over billions of years of magmatic activity. *Space Science Reviews*, *217*(1), 1–54. https://doi.org/10.1007/s11214-021-00802-1

Gaillard, F., & Scaillet, B. (2014). A theoretical framework for volcanic degassing chemistry in a comparative planetology perspective and implications for planetary atmospheres. *Earth and Planetary Science Letters*, *403*, 307–316. https://doi.org/10.1016/j.epsl.2014.07.009

Galland, O., Bertelsen, H., Eide, C., Guldstrand, F., Haug, Ø., Leanza, H. A., et al. (2018). Storage and transport of magma in the layered crust—Formation of sills and related flat-lying intrusions. In *Volcanic and igneous plumbing systems* (pp. 113–138). Elsevier.

Gargaud, M., Martin, H., López-García, P., Montmerle, T., & Pascal, R. (2013). *Young sun, early Earth and the origins of life: Lessons for astrobiology*. Springer Science & Business Media.

Gast, P. W. (1968). Trace element fractionation and the origin of tholeiitic and alkaline magma types. *Geochimica et Cosmochimica Acta*, *32*(10), 1057–1086. https://doi.org/10.1016/0016-7037(68)90108-7

Gonnermann, H. M., & Manga, M. (2007). The fluid mechanics inside a volcano. *Annual Review of Fluid Mechanics*, *39*(1), 321–356. https://doi.org/10.1146/annurev.fluid.39.050905.110207

Green, D. H., Hibberson, W. O., Kovács, I., & Rosenthal, A. (2010). Water and its influence on the lithosphere-asthenosphere boundary. *Nature*, *467*(7314), 448–451. https://doi.org/10.1038/nature09369

Grott, M., Morschhauser, A., Breuer, D., & Hauber, E. (2011). Volcanic outgassing of CO_2 and H_2O on Mars. *Earth and Planetary Science Letters*, *308*(3–4), 391–400. https://doi.org/10.1016/j.epsl.2011.06.014

Grove, T. L., & Kinzler, R. J. (1986). Petrogenesis of andesites. *Annual Review of Earth and Planetary Sciences*, *14*(1), 417–454. https://doi.org/10.1146/annurev.ea.14.050186.002221

Hammouda, T. (2003). High-pressure melting of carbonated eclogite and experimental constraints on carbon recycling and storage in the mantle. *Earth and Planetary Science Letters*, *214*(1–2), 357–368. https://doi.org/10.1016/s0012-821x(03)00361-3

Hartley, M. E., Maclennan, J., Edmonds, M., & Thordarson, T. (2014). Reconstructing the deep CO_2 degassing behaviour of large basaltic fissure eruptions. *Earth and Planetary Science Letters*, *393*, 120–131. https://doi.org/10.1016/j.epsl.2014.02.031

Hauri, E. H., Gaetani, G. A., & Green, T. H. (2006). Partitioning of water during melting of the Earth's upper mantle at H_2O-undersaturated conditions. *Earth and Planetary Science Letters*, *248*(3–4), 715–734. https://doi.org/10.1016/j.epsl.2006.06.014

Helo, C., Longpré, M.-A., Shimizu, N., Clague, D. A., & Stix, J. (2011). Explosive eruptions at mid-ocean ridges driven by CO_2-rich magmas. *Nature Geoscience*, *4*(4), 260–263. https://doi.org/10.1038/ngeo1104

Holloway, J. R. (1976). Fluids in the evolution of granitic magmas: Consequences of finite CO_2 solubility. *The Geological Society of America Bulletin*, *87*(10), 1513–1518. https://doi.org/10.1130/0016-7606(1976)87<1513:fiteog>2.0.co;2

Holloway, J. R. (1981). Volatile interactions in magmas. In *Thermodynamics of minerals and melts* (pp. 273–293). Springer.

Holloway, J. R. (1998). Graphite-melt equilibria during mantle melting: Constraints on CO_2 in MORB magmas and the carbon content of the mantle. *Chemical Geology*, *147*(1–2), 89–97. https://doi.org/10.1016/s0009-2541(97)00174-5

Holloway, J. R., & Blank, J. G. (1994). Application of experimental results to COH species in natural melts. *Reviews in Mineralogy*, *30*. 187–187.

Holloway, J. R., Pan, V., & Gudmundsson, G. (1992). High-pressure fluid-absent melting experiments in the presence of graphite: Oxygen fugacity, ferric/ferrous ratio and dissolved CO_2. *European Journal of Mineralogy*, *4*(1), 105–114. https://doi.org/10.1127/ejm/4/1/0105

Holtzman, R., Szulczewski, M. L., & Juanes, R. (2012). Capillary fracturing in granular media. *Physical Review Letters*, *108*(26), 264504. https://doi.org/10.1103/physrevlett.108.264504

Hynes, A. (2005). Buoyancy of the oceanic lithosphere and subduction initiation. *International Geology Review*, *47*(9), 938–951. https://doi.org/10.2747/0020-6814.47.9.938

Iacono-Marziano, G., Morizet, Y., Le Trong, E., & Gaillard, F. (2012). New experimental data and semi-empirical parameterization of H_2O–CO_2 solubility in mafic melts. *Geochimica et Cosmochimica Acta*, *97*, 1–23. https://doi.org/10.1016/j.gca.2012.08.035

Iwamori, H. (1998). Transportation of H_2O and melting in subduction zones. *Earth and Planetary Science Letters*, *160*(1–2), 65–80. https://doi.org/10.1016/s0012-821x(98)00080-6

Iwamori, H. (2004). Phase relations of peridotites under H_2O-saturated conditions and ability of subducting plates for transportation of H_2O. *Earth and Planetary Science Letters*, *227*(1–2), 57–71. https://doi.org/10.1016/j.epsl.2004.08.013

Iwamori, H. (2007). Transportation of H_2O beneath the Japan arcs and its implications for global water circulation. *Chemical Geology*, *239*(3–4), 182–198. https://doi.org/10.1016/j.chemgeo.2006.08.011

Jain, C., Rozel, A. B., Tackley, P. J., Sanan, P., & Gerya, T. V. (2019). Growing primordial continental crust self-consistently in global mantle convection models. *Gondwana Research*, *73*, 96–122. https://doi.org/10.1016/j.gr.2019.03.015

Keppler, H., Wiedenbeck, M., & Shcheka, S. S. (2003). Carbon solubility in olivine and the mode of carbon storage in the Earth's mantle. *Nature*, *424*(6947), 414–416. https://doi.org/10.1038/nature01828

Kiseeva, E. S., Litasov, K. D., Yaxley, G. M., Ohtani, E., & Kamenetsky, V. S. (2013). Melting and phase relations of carbonated eclogite at 9–21 GPa and the petrogenesis of alkali-rich melts in the deep mantle. *Journal of Petrology*, *54*(8), 1555–1583. https://doi.org/10.1093/petrology/egt023

Kite, E. S., Manga, M., & Gaidos, E. (2009). Geodynamics and rate of volcanism on massive Earth-like planets. *The Astrophysical Journal*, *700*(2), 1732–1749. https://doi.org/10.1088/0004-637x/700/2/1732

Lambert, I., & Wyllie, P. (1972). Melting of gabbro (quartz eclogite) with excess water to 35 kilobars, with geological applications. *The Journal of Geology*, *80*(6), 693–708. https://doi.org/10.1086/627795

Lammer, H., Kasting, J. F., Chassefière, E., Johnson, R. E., Kulikov, Y. N., & Tian, F. (2008). Atmospheric escape and evolution of terrestrial planets and satellites. *Space Science Reviews*, *139*(1–4), 399–436. https://doi.org/10.1007/s11214-008-9413-5

Lee, C.-T. A., & Lackey, J. S. (2015). Global continental arc flare-ups and their relation to long-term greenhouse conditions. *Elements*, *11*(2), 125–130. https://doi.org/10.2113/gselements.11.2.125

Lee, C.-T. A., Lenardic, A., Cooper, C. M., Niu, F., & Levander, A. (2005). The role of chemical boundary layers in regulating the thickness of continental and oceanic thermal boundary layers. *Earth and Planetary Science Letters*, *230*(3–4), 379–395. https://doi.org/10.1016/j.epsl.2004.11.019

Lesher, C. E., & Spera, F. J. (2015). Thermodynamic and transport properties of silicate melts and magma. In *The encyclopedia of volcanoes* (pp. 113–141). Elsevier.

Lesne, P., Scaillet, B., Pichavant, M., & Beny, J.-M. (2011b). The carbon dioxide solubility in alkali basalts: An experimental study. *Contributions to Mineralogy and Petrology*, *162*(1), 153–168. https://doi.org/10.1007/s00410-010-0585-0

Li, Z.-X. A., & Lee, C.-T. A. (2004). The constancy of upper mantle fO_2 through time inferred from V/Sc ratios in basalts. *Earth and Planetary Science Letters*, *228*(3–4), 483–493. https://doi.org/10.1016/j.epsl.2004.10.006

Lourenço, D. L., Rozel, A. B., Ballmer, M. D., & Tackley, P. J. (2020). Plutonic-squishy lid: A new global tectonic regime generated by intrusive magmatism on Earth-like planets. *Geochemistry, Geophysics, Geosystems*, *21*(4), e2019GC008756. https://doi.org/10.1029/2019gc008756

Lourenço, D. L., Rozel, A. B., Gerya, T., & Tackley, P. J. (2018). Efficient cooling of rocky planets by intrusive magmatism. *Nature Geoscience*, *11*(5), 322–327. https://doi.org/10.1038/s41561-018-0094-8

McKay, D. I. A., Tyrrell, T., Wilson, P. A., & Foster, G. L. (2014). Estimating the impact of the cryptic degassing of Large Igneous Provinces: A mid-Miocene case-study. *Earth and Planetary Science Letters*, *403*, 254–262. https://doi.org/10.1016/j.epsl.2014.06.040

Menand, T. (2011). Physical controls and depth of emplacement of igneous bodies: A review. *Tectonophysics*, *500*(1–4), 11–19. https://doi.org/10.1016/j.tecto.2009.10.016

Michael, P. (1995). Regionally distinctive sources of depleted MORB: Evidence from trace elements and H_2O. *Earth and Planetary Science Letters*, *131*(3–4), 301–320. https://doi.org/10.1016/0012-821x(95)00023-6

Michael, P. J. (1988). The concentration, behavior and storage of H_2O in the suboceanic upper mantle: Implications for mantle metasomatism. *Geochimica et Cosmochimica Acta*, *52*(2), 555–566. https://doi.org/10.1016/0016-7037(88)90110-x

Miller, S. L. (1953). A production of amino acids under possible primitive Earth conditions. *Science*, *117*(3046), 528–529. https://doi.org/10.1126/science.117.3046.528

Moore, L. R., Gazel, E., Tuohy, R., Lloyd, A. S., Esposito, R., Steele-MacInnis, M., et al. (2015). Bubbles matter: An assessment of the contribution of vapor bubbles to melt inclusion volatile budgets. *American Mineralogist*, *100*(4), 806–823. https://doi.org/10.2138/am-2015-5036

Murphy, D. T., Wiemer, D., Bennett, V. C., Spring, T., Trofimovs, J., & Cathey, H. E. (2021). Paleoarchean variole-bearing metabasalts from the East Pilbara Terrane formed by hydrous fluid phase exsolution and implications for Archean greenstone belt magmatic processes. *Precambrian Research*, *357*, 106114. https://doi.org/10.1016/j.precamres.2021.106114

Mysen, B. O., & Richet, P. (2018). *Silicate glasses and melts*. Elsevier.

Nakagawa, T., & Iwamori, H. (2017). Long-term stability of plate-like behavior caused by hydrous mantle convection and water absorption in the deep mantle. *Journal of Geophysical Research: Solid Earth*, *122*(10), 8431–8445. https://doi.org/10.1002/2017jb014052

Nakagawa, T., Nakakuki, T., & Iwamori, H. (2015). Water circulation and global mantle dynamics: Insight from numerical modeling. *Geochemistry, Geophysics, Geosystems*, *16*(5), 1449–1464. https://doi.org/10.1002/2014gc005701

Nava, A. H., Black, B. A., Gibson, S. A., Bodnar, R. J., Renne, P. R., & Vanderkluysen, L. (2021). Reconciling early Deccan Traps CO_2 outgassing and pre-KPB global climate. *Proceedings of the National Academy of Sciences*, *118*(14). https://doi.org/10.1073/pnas.2007797118

Newman, S., & Lowenstern, J. B. (2002). Volatilecalc: A silicate melt–H_2O–CO_2 solution model written in visual basic for excel. *Computers & Geosciences*, *28*(5), 597–604. https://doi.org/10.1016/s0098-3004(01)00081-4

Noack, L., Breuer, D., & Spohn, T. (2012). Coupling the atmosphere with interior dynamics: Implications for the resurfacing of Venus. *Icarus*, *217*(2), 484–498. https://doi.org/10.1016/j.icarus.2011.08.026

Noack, L., Höning, D., Rivoldini, A., Heistracher, C., Zimov, N., Journaux, B., et al. (2016). Water-rich planets: How habitable is a water layer deeper than on Earth? *Icarus*, *277*, 215–236. https://doi.org/10.1016/j.icarus.2016.05.009

Noack, L., Rivoldini, A., & Van Hoolst, T. (2017). Volcanism and outgassing of stagnant-lid planets: Implications for the habitable zone. *Physics of the Earth and Planetary Interiors*, *269*, 40–57. https://doi.org/10.1016/j.pepi.2017.05.010

Oppenheimer, J., Rust, A. C., Cashman, K. V., & Sandnes, B. (2015). Gas migration regimes and outgassing in particle-rich suspensions. *Frontiers in Physics*, *3*, 60. https://doi.org/10.3389/fphy.2015.00060

Ortenzi, G., Noack, L., Sohl, F., Guimond, C., Grenfell, J., Dorn, C., et al. (2020). Mantle redox state drives outgassing chemistry and atmospheric composition of rocky planets. *Scientific Reports*, *10*(1), 1–14. https://doi.org/10.1038/s41598-020-67751-7

Papale, P. (1997). Modeling of the solubility of a one-component H_2O or CO_2 fluid in silicate liquids. *Contributions to Mineralogy and Petrology*, *126*(3), 237–251. https://doi.org/10.1007/s004100050247

Papale, P. (1999). Modeling of the solubility of a two-component H_2O + CO_2 fluid in silicate liquids. *American Mineralogist*, *84*(4), 477–492. https://doi.org/10.2138/am-1999-0402

Parfitt, L., & Wilson, L. (2008). *Fundamentals of physical volcanology*. John Wiley & Sons.

Parmigiani, A., Degruyter, W., Leclaire, S., Huber, C., & Bachmann, O. (2017). The mechanics of shallow magma reservoir outgassing. *Geochemistry, Geophysics, Geosystems*, *18*(8), 2887–2905. https://doi.org/10.1002/2017gc006912

Parmigiani, A., Huber, C., & Bachmann, O. (2014). Mush microphysics and the reactivation of crystal-rich magma reservoirs. *Journal of Geophysical Research: Solid Earth*, *119*(8), 6308–6322. https://doi.org/10.1002/2014jb011124

Petraske, A. K., Hodge, D. S., & Shaw, R. (1978). Mechanics of emplacement of basic intrusions. *Tectonophysics*, *46*(1–2), 41–63. https://doi.org/10.1016/0040-1951(78)90104-x

Petrelli, M., El Omari, K., Spina, L., Le Guer, Y., La Spina, G., & Perugini, D. (2018). Timescales of water accumulation in magmas and implications for short warning times of explosive eruptions. *Nature Communications*, *9*(1), 1–14. https://doi.org/10.1038/s41467-018-02987-6

Planke, S., Rasmussen, T., Rey, S. S., & Myklebust, R. (2005). Seismic characteristics and distribution of volcanic intrusions and hydrothermal vent complexes in the Vøring and Møre basins. In *Geological Society, London, Petroleum Geology Conference Series* (Vol. 6, pp. 833–844).

Rosenberg, C., & Handy, M. (2005). Experimental deformation of partially melted granite revisited: Implications for the continental crust. *Journal of Metamorphic Geology*, *23*(1), 19–28. https://doi.org/10.1111/j.1525-1314.2005.00555.x

Rosenthal, A., Hauri, E. H., & Hirschmann, M. (2015). Experimental determination of C, F, and H partitioning between mantle minerals and carbonated basalt, CO_2/Ba and CO_2/Nb systematics of partial melting, and the CO_2 contents of basaltic source regions. *Earth and Planetary Science Letters*, *412*, 77–87. https://doi.org/10.1016/j.epsl.2014.11.044

Rozel, A., Golabek, G. J., Jain, C., Tackley, P. J., & Gerya, T. (2017). Continental crust formation on early Earth controlled by intrusive magmatism. *Nature*, *545*(7654), 332–335. https://doi.org/10.1038/nature22042

Saal, A. E., Hauri, E. H., Langmuir, C. H., & Perfit, M. R. (2002). Vapour undersaturation in primitive mid-ocean-ridge basalt and the volatile content of Earth's upper mantle. *Nature*, *419*(6906), 451–455. https://doi.org/10.1038/nature01073

Sakamaki, T., Suzuki, A., Ohtani, E., Terasaki, H., Urakawa, S., Katayama, Y., et al. (2013). Ponded melt at the boundary between the lithosphere and asthenosphere. *Nature Geoscience*, *6*(12), 1041–1044. https://doi.org/10.1038/ngeo1982

Scaillet, B., & Gaillard, F. (2011). Redox state of early magmas. *Nature*, *480*(7375), 48–49. https://doi.org/10.1038/480048a

Schmidt, M. W., & Poli, S. (1998). Experimentally based water budgets for dehydrating slabs and consequences for arc magma generation. *Earth and Planetary Science Letters*, *163*(1–4), 361–379. https://doi.org/10.1016/s0012-821x(98)00142-3

Shaw, D. M. (1970). Trace element fractionation during anatexis. *Geochimica et Cosmochimica Acta*, *34*(2), 237–243. https://doi.org/10.1016/0016-7037(70)90009-8

Shcheka, S. S., Wiedenbeck, M., Frost, D. J., & Keppler, H. (2006). Carbon solubility in mantle minerals. *Earth and Planetary Science Letters*, *245*(3–4), 730–742. https://doi.org/10.1016/j.epsl.2006.03.036

Shinohara, H. (2008). Excess degassing from volcanoes and its role on eruptive and intrusive activity. *Reviews of Geophysics*, *46*(4), RG4005. https://doi.org/10.1029/2007rg000244

Sparks, R. S. J., & Huppert, H. E. (1984). Density changes during the fractional crystallization of basaltic magmas: Fluid dynamic implications. *Contributions to Mineralogy and Petrology*, *85*(3), 300–309. https://doi.org/10.1007/bf00378108

Stern, C. R., Huang, W.-L., & Wyllie, P. J. (1975). Basalt-andesite-rhyolite-H_2O: Crystallization intervals with excess H_2O and H_2O-undersaturated liquidus surfaces to 35 kilobars, with implications for magma genesis. *Earth and Planetary Science Letters*, *28*(2), 189–196. https://doi.org/10.1016/0012-821x(75)90226-5

Stixrude, L., & Lithgow-Bertelloni, C. (2011). Thermodynamics of mantle minerals - II. Phase equilibria. *Geophysical Journal International*, *184*(3), 1180–1213. https://doi.org/10.1111/j.1365-246x.2010.04890.x

Trail, D., Watson, E. B., & Tailby, N. D. (2011). The oxidation state of Hadean magmas and implications for early Earth's atmosphere. *Nature*, *480*(7375), 79–82. https://doi.org/10.1038/nature10655

Van Hoolst, T., Noack, L., & Rivoldini, A. (2019). Exoplanet interiors and habitability. *Advances in Physics: X*, *4*(1), 1630316. https://doi.org/10.1080/23746149.2019.1630316

Van Kranendonk, M. J., Bennett, V., & Hoffmann, E. (2018). *Earth's oldest rocks*. Elsevier.

Wallace, P. J. (2018). Volatile abundances in basaltic magmas and their degassing paths tracked by melt inclusions. *Minerals, Inclusions And Volcanic Processes*, *69*, 363.

Wallace, P. J., Anderson, A. T., & Davis, A. M. (1995). Quantification of pre-eruptive exsolved gas contents in silicic magmas. *Nature*, *377*(6550), 612–616. https://doi.org/10.1038/377612a0

Weinberg, R. F., & Regenauer-Lieb, K. (2010). Ductile fractures and magma migration from source. *Geology*, *38*(4), 363–366. https://doi.org/10.1130/g30482.1

Winter, J. D. (2014). *Principles of igneous and metamorphic petrology*. Pearson Education.

Workman, R. K., & Hart, S. R. (2005). Major and trace element composition of the depleted MORB mantle (DMM). *Earth and Planetary Science Letters*, *231*(1–2), 53–72. https://doi.org/10.1016/j.epsl.2004.12.005

Yaxley, G. M., Ghosh, S., Kiseeva, E. S., Mallik, A., Spandler, C., Thomson, A. R., & Walter, M. J. (2019). CO_2-rich melts in Earth. In *Deep carbon: Past to present* (pp. 129–162).

Zahnle, K., Schaefer, L., & Fegley, B. (2010). Earth's earliest atmospheres. *Cold Spring Harbor Perspectives in Biology*, *2*(10), a004895. https://doi.org/10.1101/cshperspect.a004895

Zhang, Y., Xu, Z., Zhu, M., & Wang, H. (2007). Silicate melt properties and volcanic eruptions. *Reviews of Geophysics*, *45*(4). https://doi.org/10.1029/2006rg000216